Clays and Clay Minerals (2024), **72**, e25, 1–20
doi:10.1017/cmn.2024.20

Original Paper

Determining the stoichiometric composition of Wyoming montmorillonite using improved transmission electron microscopy-energy dispersive X-ray (TEM-EDX) techniques

L.N. Warr, B.R. Thombare, R. Sudheer Kumar, M. Peltz, C. Podlech and G.H. Grathoff
Institute of Geography and Geology, University of Greifswald, D-17487 Greifswald, Germany

Abstract

Transmission electron microscopy-energy dispersive X-ray analysis (TEM-EDX) represents an effective tool for determining the stoichiometric composition of clay minerals, but the methodology is often hampered by analytical difficulties. Studies of beam-sensitive minerals, such as smectites, are associated with low count intensities and dynamic loss of cations (e.g. K^+, Na^+, and Al^{3+}), which can lead to erroneous quantifications of composition. After exploring how to minimize cation migration by reducing the beam current density to <5 pA cm^{-2}, the most reliable and consistent compositions were determined using 1 μm^2 area measurements of particles acquired in normal TEM mode where the electron beam was parallel, the degree of specimen damage was at its minimum and good acquisition intensities (>10,000 cps) were acquired. Based on 528 TEM-EDX area analyses, the composition of Wyoming montmorillonites (SWy-1, SWy-2, and SWy-3) was studied in their natural and Ca-saturated states from thin (<50 nm thick) particle aggregates lying on lacey carbon films. Overall, the TEM-EDX results confirmed the heterogeneous charge distributions of montmorillonite at the particle and sample levels. The average composition per formula unit of SWy-1 to -3 was determined as: $(Na_{0.12}Ca_{0.04}Mg_{0.03}K_{0.02})(Si_{3.91}Al_{0.09})(Al_{1.57}Mg_{0.27}Fe_{0.19})_{2.03}\ O_{10}(OH)_2 \cdot nH_2O$, where the tetrahedral and octahedral layer charges are –0.09 and –0.19 per $O_{10}(OH)_2$, respectively, and the total layer charge ranges from –0.25 to –0.30 per $O_{10}(OH)_2$ (mean of –0.28). This study demonstrates how TEM-EDX can provide new insight into the natural heterogeneities of smectite chemistry as long as adequate calibration and specimen damage control procedures are implemented.

Keywords: beam damage; chemistry; clay minerals; EDX analyses; electron microscopy; layer charge; smectite

(Received: 02 February 2024; revised: 15 April 2024; accepted: 29 April 2024)

Introduction

Transmission electron microscopy-energy dispersive X-ray analysis (TEM-EDX), otherwise known as analytical electron microscopy (AEM), represents a powerful approach for studying the crystal chemistry of clay minerals and related nanoparticles, and has been adopted in numerous studies for determining stochiometric structural formulae (Ahn and Peacor, 1986; Nieto, 2002; Cuadros et al., 2009; Hoang-Minh et al., 2019; García-Romero et al., 2021). In this context, it can be used to calculate the variable layer charge properties of smectites and the distribution of charges associated with the tetrahedral and octahedral sheets. These negative electrostatic forces are known to control particle swelling, cation exchange capacities and ion selectivity, as well as influence the rheological properties of bentonites (Christidis et al., 2006; Laird, 2006; Zou et al., 2021). Determining layer charge is also of fundamental importance for the classification of smectite minerals and the other phyllosilicate groups (Emmerich et al., 2009; Wilson et al., 2013).

Several studies using different analytical methods have shown that the distribution of layer charge in smectites and hence their ion exchange properties are characteristically heterogeneous (Lagaly and Weiss, 1975; Lagaly, 1994; Christidis, 2006). The structural formula (SF) method provides information on the distribution of charge between tetrahedral and octahedral sheets. Differences in the layer charge determined by the alkylammonium method (AAM) and the SF method have been discussed extensively and attributed to the nature of these two analytical approaches (Christidis, 2008; Kaufhold et al., 2011; Nieto et al., 2016; Christidis et al., 2023). Methods based on chemical treatments depend on the exchange of cations in the interlayer surfaces and measure the charge density related to these properties. In contrast, the SF method relies on obtaining accurate elemental concentrations without the interference from accessory minerals and provides a measurement of the total charge related to both exchangeable and permanently fixed interlayer cations (Kaufhold et al., 2011; Christidis et al., 2023). As a result of these differences, the negative layer charge properties calculated

Corresponding author: L.N. Warr; Email: warr@uni-greifswald.de
Cite this article: Warr L.N., Thombare B.R., Sudheer Kumar R., Peltz M., Podlech C., & Grathoff G.H. (2024). Determining the stoichiometric composition of Wyoming montmorillonite using improved transmission electron microscopy-energy dispersive X-ray (TEM-EDX) techniques. *Clays and Clay Minerals* **72**, e25, 1–20.
https://doi.org/10.1017/cmn.2024.20

by the SF method are commonly higher than those determined by methods relying on chemical exchange properties.

The TEM-EDX method, most commonly conducted in scanning transmission electron microscopy (STEM) mode, represents a specialized approach used to avoid contamination as analyses can be made on a particle-by-particle basis at magnifications typically >50,000×. This method encounters a range of problems associated with electron beam interactions, namely heating, electrostatic charging, ionization damage (radiolysis), and displacement damage (Egerton and Malac, 2004; Chen et al., 2020). Some early studies showed significant loss of Na and K from micas and feldspars (Ahn et al., 1986; Ahn and Peacor, 1986; van der Pluijm et al., 1988). Extensive loss of a range of cations, such as Al, Mg, Ca, K, and even Fe, was reported from spot analyses of various beam-sensitive clay minerals, such as kaolinites and smectites (Ma et al., 1998). Despite these studies, there remains little systematic research addressing EDX compositional determinations of clay minerals and how to avoid damage, while maintaining sufficient counting statistics by using spot, area or mapping analyses, particularly in the context of the availability of larger and more sensitive detectors. As a result, obtaining reliable measurements using improved instrumentation is still not a straightforward and routine procedure (Kogure, 2020).

This study presents an analytical strategy by which accurate smectite compositions are determined. It uses a large area (100 mm^2) silicon drift detector (SDD), combined with minimizing electron dosage during TEM-EDX area analyses of the basal surfaces of individual particles and particle stacks at 50,000× magnification. As a result, a more accurate insight into the compositional variations of the Wyoming montmorillonite SWy sample series from Crook County is provided, which highlights the true heterogeneity of layer charge distributions and interlayer cation content.

Composition determinations using the SF method

The SF method is a well-known procedure for calculating the stoichiometric composition of minerals and is the standard method for determining the layer charge of phyllosilicates (Newman and Brown, 1987). For smectites, SF calculations are most commonly carried out based on 11 oxygen atoms per formula unit (i.e. $O_{10}(OH)_2$ after release of H as H_2O), which corresponds to a negative electron charge of –22. Chemical analyses of the cations in clay minerals are commonly given as elemental oxides in weight % (wt.%) and the cations allocated to tetrahedral, octahedral, and interlayer sites following Pauling's rules (Newman and Brown, 1987). Firstly, for a formula unit calculation, the empty sites in the tetrahedral positions are filled with Si^{4+} and Al^{3+} to make up four cations. The remaining Al^{3+}, as well as Mg^{2+} and Fe, are assigned to octahedral sites. In the case of a montmorillonitic smectite, the iron is assumed to be Fe^{3+} unless the presence of Fe^{2+} is verified by independent methods (e.g. wet chemical, Mössbauer spectroscopy or electron energy loss spectroscopy). Finally, Ca^{2+}, Na^{+}, and K^{+} are assigned to the exchangeable interlayer sites. If Mg^{2+} is suspected to be present as an exchangeable cation, one approach is to assume that two cations occupy the octahedral site and to assign any excess Mg^{2+} to the interlayer. Alternatively, the interlayer cations may be exchanged with Ca^{2+}, in which case all Mg^{2+} can be treated as an octahedral cation. In the latter procedure, the total number of octahedral ions is not fixed at two, but may exceed this value when containing some trioctahedrally coordinated divalent metals (e.g. Mg^{2+} or Fe^{2+}). For the montmorillonite–beidellite series, calculations following the latter procedure rarely significantly exceed the total of two metal ions and range between 2.0 and 2.1 per $O_{10}(OH)_2$ (García-Romero et al., 2021). In contrast, Ca-saturated trioctahedral minerals such as saponite, stevensite, and kerolite have higher octahedral totals between 2.81 and 3.00 per $O_{10}(OH)_2$ (Wilson et al., 2013).

Based on the SF method, it has been shown that smectites in the montmorillonite to beidellite series have total layer charges that vary between –0.2 and –0.7 per $O_{10}(OH)_2$ (Wilson et al., 2013). Similarly, the layer charges of saponite and stevensite span the range of –0.18 to –0.36 per $O_{10}(OH)_2$.

Mineralogy and chemistry of the Wyoming bentonite (SWy) series

The SWy bentonite series (SWy-1, SWy-2 and SWy-3) from Crook County, Wyoming, is one of the most studied clays made available to the science community. Obtainable as part of The Clay Minerals Society source clay collection since 1972 (https://www.clays.org/sourceclays_data/), SWy-1 was first collected from the Cretaceous Upper Newcastle formation at a mine location 50 km west of Colony. Two subsequent samples (SWy-2 and SWy-3) were taken from the same location later in 1993 and 2018. This reference material is of particular importance as the commercial product, MX80 bentonite, is sourced from these mines, and is sold as various mixed blends that often vary in composition. The industrial MX80 product is commonly used in underground repository laboratories to investigate future high-grade nuclear waste storage solutions. This product has also been investigated in detail in terms of its mineralogy, chemistry, and swelling behavior (Villar, 2005; Villar et al., 2005; Perdrial and Warr, 2011; Cui, 2017).

SWy-1 contains quartz in most grain-size fractions and particularly in the coarser separates covering the 1–10 μm range where elevated SiO_2 was observed (Table 1; Fig. 1; Koster van Groos and Guggenheim, 1984). Carbonate was most enhanced in the >10 μm fraction with elevated CaO. K-feldspar was considered to be present in the 5–10 μm fraction with higher concentrations of K_2O. The <1 μm fractions contained the highest proportions of smectite, whereby the <0.1 μm was considered to represent a close to pure montmorillonite composition. It was suggested that the low concentrations of Na_2O measured in these size fractions, compared with the compositions given by van Olphen and Fripiat (1979), represented some loss of this element during fusion and cation loss from the glass sample during microprobe analysis (Koster van Groos and Guggenheim, 1984).

Qualitative assessments of the original SWy material considered the mineral assemblages of SWy-1 and SWy-2 to be equivalent (Chipera and Bish, 2001). The shipped powder of SWy-2 contained by weight 75% smectite, 8% quartz, 16% feldspar and 1% gypsum + mica and/or illite, as well as possibly some kaolinite and/or chlorite. These authors also documented in the <2 μm fraction 95% smectite, 4% quartz and 1% feldspar + gypsum + mica and perhaps kaolinite and/or chlorite. In contrast, Vogt et al. (2002) considered the <2 μm of the SWy-2 sample to contain a higher proportion of impurities (total 13.3 wt.%) that included quartz, pyroxenes, kaolinite, calcite, chlorite, and plagioclase.

No detailed quantification of the minerals in the currently available SWy-3 has so far been reported. Therefore, a quantification of the <1 μm fraction by Rietveld refinement was undertaken using Profex (Doebelin and Kleeberg, 2015). This revealed by weight 92.9±0.2% smectite, 5.3±0.2% cristobalite, 1.2±0.1% quartz and 0.7±0.1% calcite

https://doi.org/10.1017/cmn.2024.20 Published online by Cambridge University Press

Table 1. Mean chemical compositions of the various grain-size fractions of the SWy-series (SWy-1, SWy-2, SWy-3) normalized to 100% and without hydroxyls and water

Sample	Method	*n*	SiO_2	Al_2O_3	Fe_2O_3	FeO	MgO	CaO	Na_2O	K_2O
SWy–1, <2 μm[a]	XRF-EM-WC	1	67.7	20.8	4.2	0.1	3.0	1.9	1.7	0.6
SWy–1, whole[b]	EM	1	68.6	21.2	4.3	–	2.9	1.6	0.9	0.6
SWy–1, >10 μm[b]	EM	1	66.4	11.9	2.1	–	1.2	17.2	0.8	0.5
SWy–1, 5–10 μm[b]	EM	1	74.9	13.4	3.0	–	1.1	3.5	0.8	3.3
SWy–1, 2–5 μm[b]	EM	1	80.7	12.9	3.2	–	1.7	0.7	0.2	0.5
SWy–1, 1–2 μm[b]	EM	1	75.6	17.2	3.7	–	2.2	0.8	0.3	0.2
SWy–1, 0.5–1 μm[b]	EM	1	63.5	29.8	3.3	–	1.5	0.5	1.2	0.2
SWy–1, 0.2–0.5 μm[b]	EM	1	64.9	24.0	5.6	–	3.9	1.1	0.4	0.1
SWy–1, 0.1–0.2 μm[b]	EM	1	66.9	23.1	5.1	–	2.8	1.1	0.9	0.1
SWy–1, <0.1 μm[b]	EM	1	66.9	23.9	4.7	–	2.8	1.1	0.6	0.2
SWy–1-K, <0.1 μm[c]	Not stated	1	65.0	23.1	4.8	–	3.0	0.1	0.2	4.0
SWy–1-K, <2 μm[c]	Not stated	1	68.8	20.4	4.2	–	2.5	0.1	0.2	3.8
SWy–1-Ca, <2 μm[d]	Not stated	1	67.0	23.3	4.2	–	2.8	2.6	0.1	0.1
SWy–1-Na, <2 μm[e]	XRF	1	66.4	22.9	4.6	–	3.0	0.0	3.1	0.0
SWy–2, <2 μm[f]	AAS-FES	4	65.6	23.5	4.7	–	3.1	1.3	1.6	0.2
SWy–2, <2 μm[g]	XRF	1	69.1	21.5	4.5	–	4.7	0.1	–	0.1
SWy–3, <75 μm[h]	XRF	1	67.6	21.2	4.1	–	2.7	1.5	2.3	0.7

[a]van Olphen and Fripiat (1979)
[b]Koster von Groos and Guggenheim (1984)
[c]Whitney and Northrop (1988)
[d]Le Forestier et al. (2010)
[e]McKinley et al. (1995)
[f]Mermut and Cano (2001)
[g]Vogt et al. (2002)
[h]Byun et al. (2023).
EM = electron microprobe, WC = wet chemistry, AAS-FES = atomic absorption spectroscopy – flame emission spectroscopy

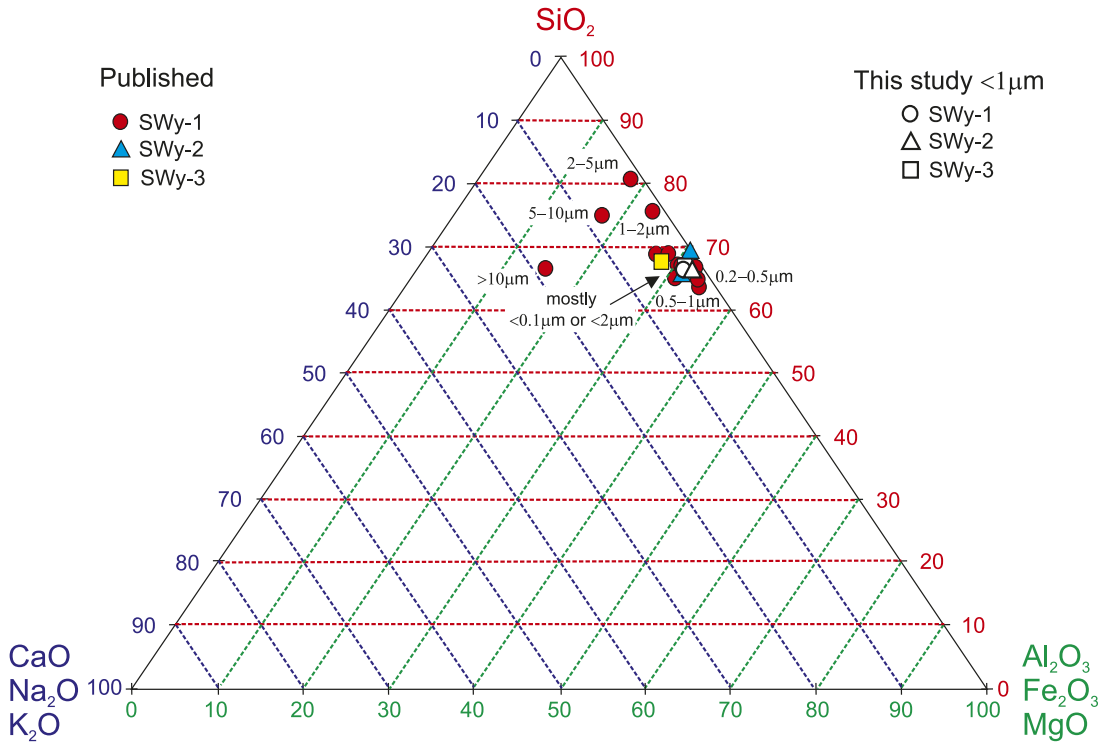

Figure 1. Ternary plot of SiO_2 *vs* $CaO+Na_2O+K_2O$ *vs* $Al_2O_3+Fe_2O_3+MgO$ (normalized to 100%) for the different grain-size fractions of the SWy-1, SWy-2, and SWy-3 sample series. Calculated from the oxide weight % data listed in Table 1. The montmorillonite compositions determined in this study are shown as open symbols.

https://doi.org/10.1017/cmn.2024.20 Published online by Cambridge University Press

(Fig. 2a). The main (101) reflection at 0.40 nm was assigned to cristobalite due to the excellent refinement result and the relatively low full-width-at-half-maximum value (0.27°2θ). A pattern using opal C/CT could not be calculated due to the lack of an available structure file but based on published results it would be expected to produce a similar refinement result (Elzea et al., 1994; Hillier and Lumsdon, 2008; Qiao et al., 2019). Some calcite was detected in the random powder of <1 μm SWy-3 and in the texture preparations of the <1 μm SWy-2 fraction, whereas no 0.40 nm reflection of opal/cristobalite was recognized in SWy-1 or SWy-2 (Fig. 2b). Additional traces of

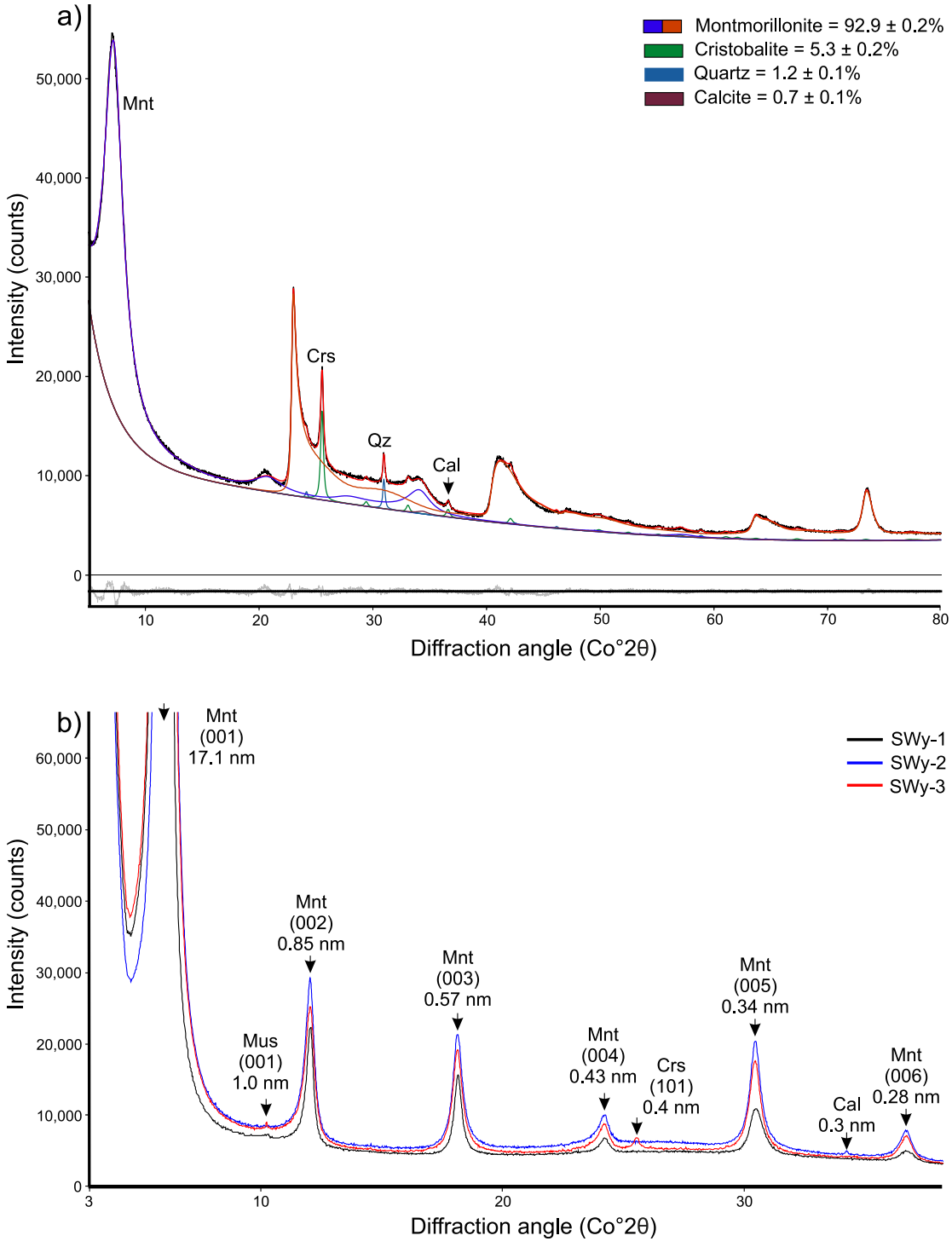

Figure 2. (a) Rietveld refinement of the X-ray diffraction pattern of a random powder preparation of the SWy-3 <1 μm fraction (after Ca-saturation) containing montmorillonite, quartz, cristobalite, and calcite. The patterns were measured using a Bruker D8 Advance diffractometer (Karlsruhe, Germany) with CoKα radiation, a Lynxeye 1D stripe detector, and primary and secondary Soller collimators. The refinement was made using Profex (Doebelin and Kleeberg, 2015). Successful quantification of the mixed water-layered structures of the dried montmorillonite required a combination of smectite and R0 illite-smectite parameter files used by Ufer et al. (2012). (b) Comparative X-ray diffraction patterns of textured preparations of the SWy1-3 series <1 μm fractions with natural cation contents after ethylene glycol treatment. Samples contain mostly montmorillonite (Mnt) with trace concentrations of muscovite (Mus), quartz (Qz), ±cristobalite (Crs) and ±calcite (Cal). IMA-approved mineral abbreviations after Warr (2020).

https://doi.org/10.1017/cmn.2024.20 Published online by Cambridge University Press

muscovite with an (001) reflection at 1.0 nm was detected in all XRD patterns of the <1 μm fractions following ethylene glycol treatment. Minor quantities of quartz were also considered to be present in all samples; however, its main 0.32 nm reflection was masked by a prominent (005) montmorillonite peak in all texture XRD patterns.

The interlayer of the Wyoming montmorillonite SWy series is known to be dominated by Na^+ ions. The interlayer cation composition of the 0.2 μm fraction of SWy-2 was reported to contain 48% Na^+, 31% Ca^{2+}, 19% Mg^{2+}, and 2% K^+ with a cation exchange capacity of 78 cmol kg^{-1} and a layer charge of –0.29 per $O_{10}(OH)_2$ determined using a single alkylammonium ion expansion (Steudel et al., 2009). Based on the adsorption of a range of alkylammonium compounds of variable molecular length, the layer charge distribution of the bulk powder sample was calculated to range between –0.2 and –0.4 per $O_{10}(OH)_2$ and have an average of –0.28 per $O_{10}(OH)_2$ (Hofmann, 2003), following the methodology of Lagaly (1994). The Fe is considered to be close to randomly distributed in the octahedral sheets in this dioctahedrally arranged structure (Finck et al., 2015). Most is present as Fe^{3+} as determined by Mössbauer spectroscopy (Bishop et al., 1999). The small amounts of Fe^{2+} measured by wet chemical methods reported by van Olphen and Fripiat (1979) may represent mineral impurities often present in the analyzed fractions. The iron state can be abiotically reduced to the Fe^{2+} during Fe^{2+} adsorption from solution where the rate of the reaction is considered to be fast due to electron transfer across the oxygen sheets (Latta et al., 2017).

Based on its crystal chemistry, this smectite is considered to represent a low-charge cis-vacant beidellitic montmorillonite (Derkowski and Kuligiewicz, 2017). A range of stoichiometric formulae has been presented for the SWy series, albeit largely based on non-pure powders. From these studies, a generalized structural formula can be written with the ranges of: $(Na, Ca, Mg, K)_{0.25\text{-}0.45}(Si_{3.79\text{-}3.96}Al_{0.04\text{-}0.21})\ (Al_{1.52\text{-}1.58}Mg_{0.23\text{-}0.32}Fe_{0.20\text{-}0.23})_2\ O_{10}\ (OH)_2 \cdot nH_2O$. This corresponds with a total layer charge between –0.25 and –0.45 per $O_{10}(OH)_2$, a tetrahedral charge ranging from –0.04 to –0.29 per $O_{10}(OH)_2$ and an octahedral charge from –0.19 to –0.30 per $O_{10}(OH)_2$.

Materials and methods

Sample purification and cation exchange

Based on our laboratory experience working with the SWy sample series, it is experimentally challenging to produce a 100% pure smectite specimen using grain-size separation techniques. The finest fractions usually contain traces of mica, quartz, calcite and, in the case of SWy-3, cristobalite (Fig. 2). Purifying large quantities of clay in its natural form from bulk materials may also lead to cation exchange reactions as the material comes into contact with water. Where calcite is present, as in the coarser fractions of the SWy material, some exchange of Na^+ by Ca^{2+} is likely due to the dissolution of this mineral. If sulfates are also present, such as those produced by the oxidation of pyrite, then gypsum might precipitate when concentrating the solid clay during drying at 60°C in an oven.

In this study, a TEM-EDX specimen preparation protocol was developed that maximized the concentration of smectite, while maintaining either its original mixed cation interlayer chemistry or by achieving a close to homoionic state by exchange treatment with $CaCl_2$. For preparing natural samples (SWy-Natl), 75 mg of bentonite powder was taken from the stocks of homogenized SWy-1, SWy-2, and SWy-3 source clays, and each suspended in 10 mL of ethanol (≥96% grade supplied by Carl Roth, Karlsruhe, Germany) contained in glass vials. Ethanol was used instead of water to reduce the mobility of the exchangeable cations (Cui et al., 2023). To include the heterogeneity of each batch, five random samples were prepared from each stock. The clay was first mixed on a shaking table and then dispersed in a Sonotex ultrasonic bath at 35 kHz (Bandelin-Electronic, Berlin, Germany). An additional set of samples was prepared in the same way using double-distilled water. The second set was placed in dialysis bags and exchanged with 0.1 M $CaCl_2$ solution five times over a period of 5 days, combined with intermittent ultrasonic bath treatment. These solutions were then washed by dialysis in distilled water until all chloride salts were removed, after which the solutions were returned to their vials. These fractions were labeled Ca-saturated Wyoming clay (SWy-Ca).

TEM preparation

To obtain the <1 μm particle size fractions of SWy-Natl samples in ethanol and SWy-Ca samples in water, the clay-in-suspension was left to sediment for 3 h 30 min, and 5 h, respectively. These sedimentation rates were calculated using Stokes' law after considering differences in solution density, viscosity, and particle density. As the Ca-saturated samples were cation exchanged five times and only 0.1–0.4 wt.% Na_2O remained compared with 2.3–2.7% CaO, it is considered that little or no segregation of montmorillonite particles occurred based on interlayer content. Following sedimentation, the 0.50 mL of solution was extracted from the upper 10 mm solution and diluted in 10 mL of ethanol or water before ultrasonic dispersion. A few drops of <1 μm suspension were then placed on a lacey carbon film (300-mesh from Science Services GmbH, München, Germany) stretched over a gold grid by flooding the substrate and then left to dry. No carbon or metal coating of the specimen was considered necessary. This preparation technique produced dispersed and scattered smectite particles and aggregates of particles located over the holes and the carbon film that were most commonly oriented with their basal surfaces parallel to the film. Occasional particles lying over the holes were oriented perpendicular to the film, from which basal lattice layers and packet thicknesses could be imaged and measured. The smectite particles and clusters of particles in the c-direction were typically 5–50 nm thick.

TEM-EDX analyses

Analyses were carried out using a JEOL 2100 Plus TEM microscope (Tokyo, Japan) housed at the mineralogical laboratories of the University of Greifswald, Germany. The instrument has a LaB6 filament and is operated at a high-tension acceleration voltage of 200 kV, which under ideal conditions yields a 0.14 nm point resolution. The microscope is equipped with an energy-dispersive X-ray spectrometer (Oxford Instruments AZtecEnergy Ultim Max TLE System from Wiesbaden, Germany) and a large 100 mm^2 SDD surface. For quantitative analysis, data were collected from thin homogeneous areas typically 1 μm^2 in size that could be imaged by TEM and satisfy the thin-film criterion of Lorimer and Cliff (1976). The thicknesses of the particles selected were <50 nm where the effects of adsorption and fluorescence are considered to be minimal (Bourdelle et al., 2012). The software allowed adjustments to be made for specimen thickness and mineral density. For montmorillonite particles, the thickness was set at 10 nm and the

https://doi.org/10.1017/cmn.2024.20 Published online by Cambridge University Press

dry density at 2.76 g cm^{-3}. Varying the thickness correction between 10 and 50 nm had no effects on the calculations made. All EDX analyses were conducted using a beam current of 101.7 μA, an energy range of 0–10 keV, magnifications of 50,000×, spot size 1 and a time constant of 4 or 6 (see Table S1 in the Supplementary material). During analyses, the beam current density was always maintained below 5 pA cm^{-2} to minimize specimen damage.

Acquisition intensity and beam damage characterization

The effects of acquisition intensity and beam damage were first established by collecting time-dependent chemical compositions over 90 s using (i) spot analysis (spot size 1 or a beam width of ~25 nm), (ii) area analyses with a 1×1 μm square window, and (iii) equivalent sized area analyses using the EDX element mapping software. The elemental mapping in STEM mode used a camera length of 10 cm with 2048 channels and a 512-point resolution. The dwell time per point selected was 10 μs, which at the given beam settings corresponded to an electron dose of approximately 78,932 electrons per $Å^2$. A similar elemental mapping approach has been previously adopted in SEM-EDX studies of smectites in bentonites (Podlech et al., 2021; Sudheer Kumar et al., 2021) as well as in TEM-EDX investigations of phyllosilicates minerals (Wang et al., 2019). As EDX mapping could not be undertaken in TEM mode, the mapping software was used to make a higher resolution area analysis with a higher time constant of 6 and an increased number of channels (2048). All time-dependent data were acquired using the real-time mode of the Oxford AZtecEnergy software where an updated chemical composition was calculated with a refresh time of 1 s. It is assumed that any delay between acquisition and calculation was consistent between each refresh time. This approach provided an accurate record of the changes related to the measured intensities, the counting statistics and specimen beam damage effects.

Measurements showed that significant fluctuations occurred in most analyses with <50 s of acquisition time (Fig. 3). These variations were attributable to insufficient counting statistics. The most consistent values were obtained in TEM mode (Fig. 3a–c), which reached intensity acquisition rates of 10,000 and 20,000 counts per second (cps). For spot analyses, the lower concentrations of Na, Ca, and K did not level off during the entire 90 s of measurement time, whereas the area analysis stabilized after 50 s and in the higher resolution area analysis after just 20 s. None of these measurement procedures in TEM mode showed signs of a cation loss due to beam damage at 50,000× magnification when using these instrumental settings.

Elemental compositions acquired in STEM mode showed more time-dependent variants than TEM mode measurements (Fig. 3d–f). Significant fluctuations occurred in Na, Ca, and K, as well as Fe and Mg during the 90 s of measurement time. Only in mapping mode were more consistent values of Ca and K measured after 60 s although Na and Mg continued to fluctuate. Overall, the low intensities of 2000 and 5000 cps were considered insufficient for obtaining precise measurements and would require significantly longer acquisition times.

At a higher magnification of 100,000×, some thin montmorillonite particles showed clear signs of beam damage-induced variations (Fig. 4). Significant decreases in the concentrations of K, Ca as well as Fe, Mg, and Al indicate that these cations were mobile under these conditions and migrated out of the electron beam, whereas Si remained in place and relatively increased its concentration as the other elements were lost. The Na was only detected after 18 s count time due to the low intensities of this peak, which resulted in variable concentrations probably due to difficulties in distinguishing it from the background and the tails of the neighbouring Mg peak. Na was also likely lost in the electron beam under these conditions.

Determination of k-factors and calibration

To attain accurate EDX results, the instrumental k-factors were adjusted using a set of phyllosilicate standards of known elemental composition. For this purpose, specimens of kaolinite, biotite, phlogopite, and vermiculite were prepared. In addition, pure prehnite, orthoclase, and epidote were used for calibrating Na and Ca. These crystals were first disaggregated by dry grinding to a powder in an agate ball mill for <5 min and then ultrasonically treated as a suspension in water for several hours to further break up and delaminate particles. As the grinding time was short, no significant Si contamination of the material is considered to have occurred. The <1 μm fraction was then separated by sedimentation and pipetted onto a lacey carbon film in the same way as the SWy sample series. TEM-EDX measurements were only obtained from very thin particles to avoid absorption or fluorescence effects.

The homogeneity of these minerals was first checked by TEM-EDX analysis by dispersion and sedimentation of 75 mg of each sample in ethanol following the same standard procedure as described for the clay preparations. The major element compositions of the minerals were determined by X-ray fluorescence (XRF) fusing 800 mg of dry powder and measuring using a Philips W2404 X-ray spectrometer. The mass loss was measured after heating to 105°C (20 h) and 1050°C (1 h) to determine the loss on ignition (LOI). The remaining sample was melted with a flux ($LiBO_2$+$Li_2B_4O_7$) at ~1100°C to prepare the tablet used for measurement. The accuracy of measurements was controlled using USGS standards (e.g. BHVO-2, AGV-2, and RGM-1) available from the Geology, Geophysics, Geochemistry Science Center (Lakeword, CO, USA).

The 12 pure mineral standards chosen (Table S2 in the Supplementary material) contained high concentrations of the measured elements: namely kaolinite for Al, biotite for Fe, vermiculite and phlogopite for Mg, epidote and prehnite for Ca, muscovite, biotite, and phlogopite for K, and oligoclase for Na. First, Al was calibrated by adjusting its k-value to 0.995 using the two kaolinite standards KGa1b and KGa2 to produce a SiO_2:Al_2O_3 ratio of 1.12, which is equivalent to the known ratios for these minerals (1.12 and 1.14, respectively; Mermut and Cano, 2001). The overall quality of the calibrations was tested by plotting the oxide weight % values determined by the particle-by-particle measurements of the TEM-EDX method against the bulk mineral powders measured by XRF measurements (Fig. 5). Following appropriate adjustment of the k-values (Al 0.995, Fe 1.380, Mg 0.990, Ca 1.100, K 1.150, and Na 1.088), an excellent 1:1 correlation (R^2=0.999) was attained between the TEM-EDX and XRF measured compositions. These oxide results were used to determine the average analytical accuracy (in absolute wt.%) of SiO_2±0.5 in the range of 39–51, Al_2O_3±0.6 in the range of 11–47, Fe_2O_3±0.8 in the range of 6–28, Fe_2O_3±0.4 in the range of 1–3, MgO±0.4 in the range of 1–31, CaO±0.4 in the range of 4–28, K_2O±0.6 in the range of 1–11, and Na_2O±0.01 in the range of 6–9. All elemental oxides under 1 wt.% are considered to have an absolute accuracy of ±0.2 wt.%. Below <0.1% wt.%, concentrations could not be reliably determined but were nevertheless measured when detected.

https://doi.org/10.1017/cmn.2024.20 Published online by Cambridge University Press

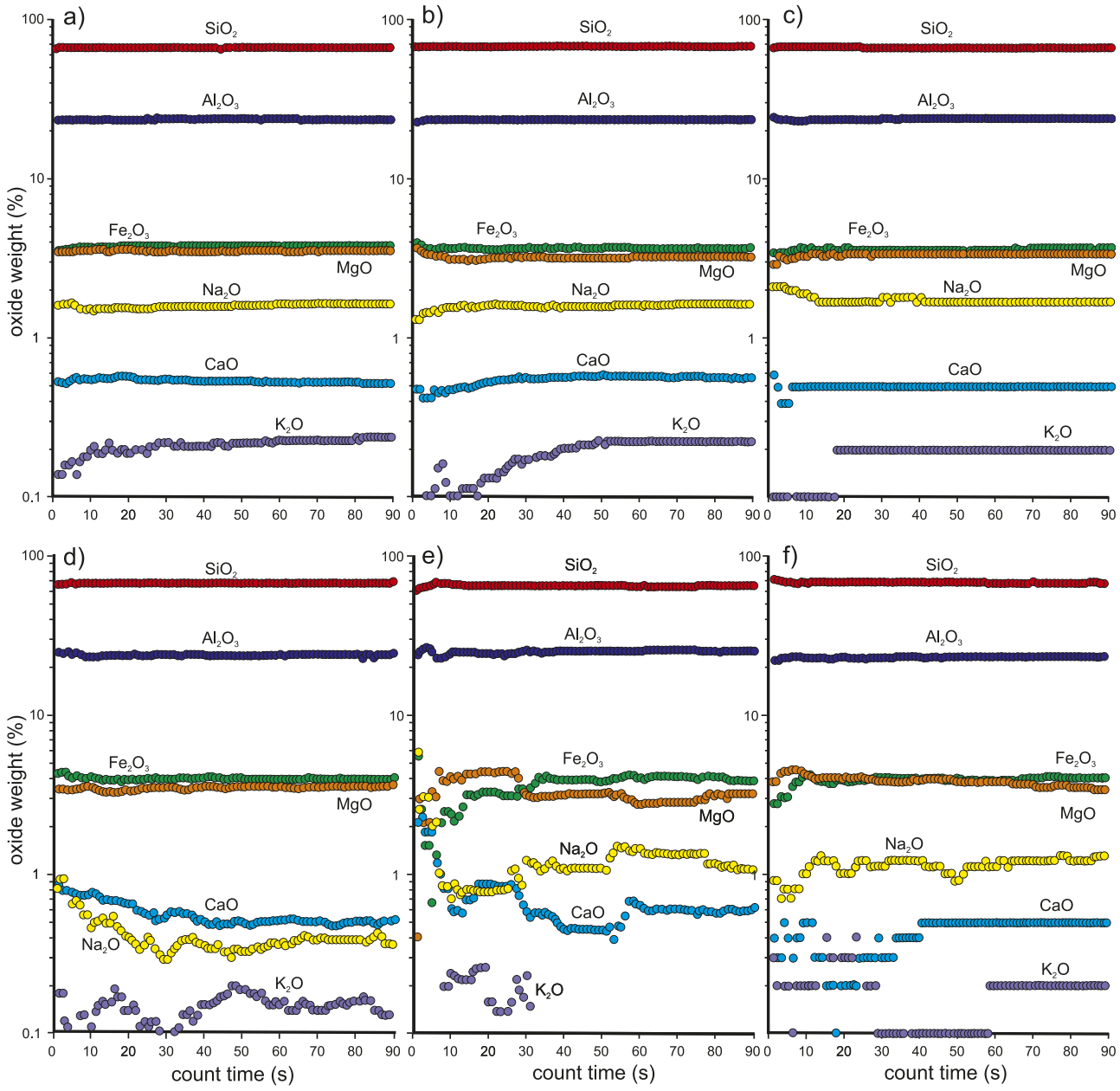

Figure 3. TEM-EDX-determined elemental concentrations (expressed as oxide wt.) *vs* count time (s) for selective montmorillonite particles based on (a) spot analysis in TEM mode, (b) area analysis in TEM mode, (c) higher-resolution area analysis using the mapping option in TEM mode, (d) spot analysis in STEM mode, (e) area analysis in STEM mode, and (f) mapping analysis in STEM mode. All measurements were made at 50,000× magnification using the setting listed in Table S1 (see Supplementary material). For point and area TEM mode analyses, the count rates obtained using a time constant of 4 or 6 ranged between 10,000 and 20,000 cps with dead times of 2–3%. For STEM mode analyses using a time constant of 4, the count rates ranged between 2000 and 5000 cps with deadtimes of 1–3%. The disappearance of K_2O after ~30 s in panel (c) was due to the inability of the software to detect this elemental peak below certain detection limits.

Determining the composition of SWy montmorillonites and SF calculations

Following the adjustment of the k-factors, the composition of montmorillonite particles was determined using area analysis (1 μm^2) in TEM-EDX mode, which presented a reliable and faster way of acquiring measurements. The average compositions of the non-cation exchanged samples were determined by multiple analyses (n=149–154). The reliability of these measurements was then cross-checked against SEM-EDX mapping of the same grain-size fractions along with selective XRF analyses of two samples (Table 2). These were in good agreement, despite traces of some other minerals (quartz, cristobalite, calcite, and mica) known to be present in the powder samples used for SEM and XRF study (Fig. 2). During the acquisition of the TEM-EDX data, accessory minerals could be recognized and avoided during the analysis of the montmorillonite particles.

Structural formulae were determined from atomic concentration ratios whereby only the elements known to occur in montmorillonite were included in the calculations, i.e. (in order of increasing atomic number) Na, Mg, Al, Si, K, Ca, and Fe. Carbon from the lacey grid film was excluded and its presence did not hinder the accurate measurement of the elements of interest. The structural formulae of the montmorillonites were calculated based on $O_{10}(OH)_2$ i.e. 11 oxygen

https://doi.org/10.1017/cmn.2024.20 Published online by Cambridge University Press

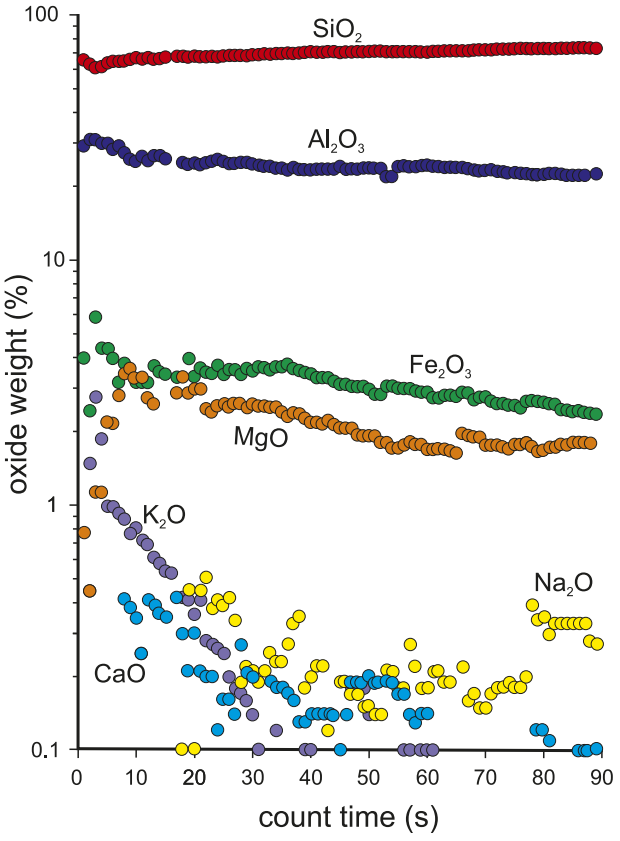

Figure 4. TEM-EDX determined elemental concentrations (expressed as oxide wt.%) *vs* count time (s) for a selected montmorillonite particle measured in TEM mode by area analysis. The decreasing concentrations of many elements with time indicate specimen damage and migration out of the electron beam. Measurement parameters were 100,000×, count input ~10,000 cps, deadtime 2–3% and a time constant of 4.

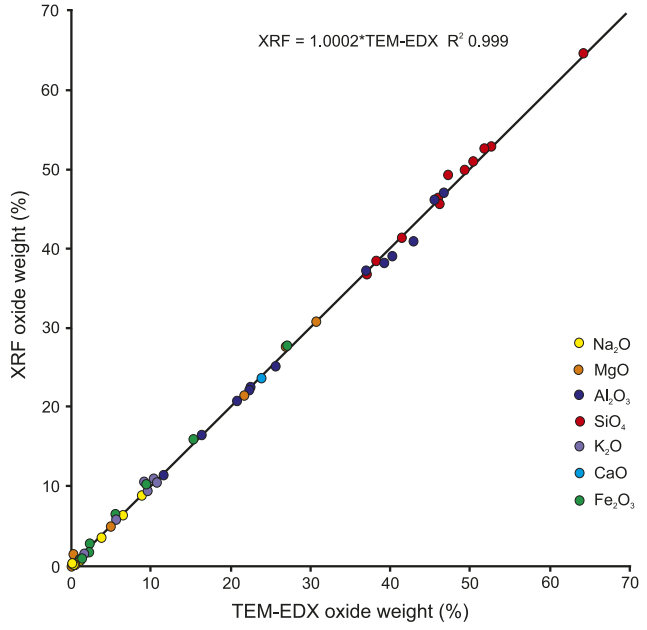

Figure 5. TEM-EDX particle measurements *vs* XRF bulk powder measurements of the elements contained in the 12 pure minerals used for calibration purposes (data provided in Table S2 in the Supplementary material). Elemental concentration expressed as oxide wt.%.

anion equivalent. As the oxidation state is not determined by routine EDX analysis, all the Fe present was considered as Fe^{3+}. Therefore, the presence of some Fe^{2+} could not be excluded. The amount of Mg^{2+} in the interlayer and octahedral sites was established by analyzing Ca-exchanged samples (Tables 2 and 3). Based on these results, it was assumed that all Mg^{2+} in exchanged samples was removed from the interlayer and that all detectable Mg^{2+} represents that located in octahedral sites. For calculations, the sum of all octahedral cations was not fixed at 2 and after summing $^{VI}Al^{3+}$, Fe^{3+}, and Mg^{2+} it reached values of 2.02 or 2.03 for the different Ca-exchanged SWy samples. The formulae of the natural SWy series were then determined by first allocating Mg^{2+} to the octahedral sites until totals of 2.02 and 2.03 were reached and then placing the remaining Mg^{2+} into the interlayer. The concentrations of elements close to the detection limit of ~0.10 wt.% corresponded to 0.01 $O_{10}(OH)_2$, whereas those below the detection limit were given as 0.00 (Table 4).

All calculation steps used for the determination of the structural formulae are given in the Supplementary material spreadsheet file (Table S2).

Results

TEM observations

Stacked aggregated montmorillonite particles, also known as tactoids, were easy to recognize in TEM images at magnifications of 50,000× due to their light gray appearance representing very thin sheets typically <50 nm in thickness (Fig. 6a). These thin flat aggregates as well as single coherent particles were those that were measured by EDX analyses. The aggregates were usually made up of individual particles tens to hundreds of nanometers in width in the a–b dimension that had straight to curved edges (Figs 6a and 7a). Hexagonal or lath shapes were distinguishable, indicating that they represent crystal shapes formed by crystal growth. These were stacked on top of each other with very low-angle discontinuities between them (Fig. 7b). Electron diffraction patterns indicated these small crystals (hereafter referred to as crystallites after Warr and Nieto, 1998) contained well-ordered lattice layers that formed distinct diffraction spots rather than streaks (Fig. 6b). These crystallites were randomly stacked on top of each other to produce numerous diffraction spots that defined prominent (hkl) rings corresponding to d-values and Miller indices of 4.5 Å (020) (110), 2.6 Å (130) (200) and 1.5 Å (060) (330).

The individual montmorillonite crystallites making up the aggregates were not always distinguishable due to their thinness and low contrast features. In SWy-1, some very small hexagonal crystals, tens of nanometers in size, were observed, which indicated that nucleation occurred on the surfaces of the larger aggregates (Fig. 7a). The aggregates were often bordered by montmorillonite particles that lay subvertical, where crystallite thicknesses could be measured (Fig. 7b). High-resolution imaging of the particle edges revealed very thin sheets consisting most commonly of 2–6 coherently stacked lattice layers (Fig. 7b–d). The lattice thickness was typically 1.2 nm, indicating that one water layer or residual ethanol was still present in the interlayer under the vacuum of the microscope. In contrast, the flat montmorillonite crystals were most commonly characterized by lattice fringes of 0.45 nm, representative of a (020) lattice plane (Fig. 7b). Upon closer examination, the discontinuities between packets were often characterized by layer terminations that probably represented the location of edge dislocations (Fig. 7c).

https://doi.org/10.1017/cmn.2024.20 Published online by Cambridge University Press

Table 2. Mean chemical compositions of the <1 μm size fractions of the SWy-series (SWy-1, SWy-2, SWy-3) measured in our laboratory by TEM-EDX, SEM-EDX, and XRF

Sample	Method	*n*	SiO_2	Al_2O_3	Fe_2O_3	FeO	MgO	CaO	Na_2O	K_2O
SWy–1-Natl, <1 μm	TEM-EDX	151	66.3	23.8	4.4	–	3.6	0.6	1.1	0.3
SWy–2-Natl, <1 μm	TEM-EDX	154	66.2	24.4	4.3	–	3.5	0.6	0.8	0.3
SWy–3-Natl, <1 μm	TEM-EDX	149	66.7	24.1	3.9	–	3.3	0.6	1.3	0.2
SWy–1-Ca, <1 μm	TEM-EDX	24	66.5	24.0	4.2	–	3.0	2.1	0.1	0.1
SWy–2-Ca, <1 μm	TEM-EDX	26	66.0	24.3	4.2	–	3.1	2.0	0.3	0.1
SWy–3-Ca, <1 μm	TEM-EDX	24	66.9	24.5	3.8	–	3.0	1.8	0.2	0.1
SWy–2, <1 μm	XRF	5	65.5	23.1	4.6	–	3.2	1.4	2.1	0.2
SWy–3-Ca, <1 μm*	XRF	5	67.7	22.8	4.3	–	2.5	2.6	0.1	0.1
SWy–1, <1 μm	SEM	5	66.4	21.8	4.8	–	3.7	0.6	2.6	0.1
SWy–2, <1 μm	SEM	5	66.5	22.1	4.7	–	3.6	0.7	2.2	0.2
SWy–3, <1μm*	SEM	5	67.8	21.1	4.6	–	3.5	0.7	2.1	0.2
SWy–1-Ca, <1 μm	SEM	5	66.3	22.8	4.5	–	4.5	2.3	0.4	0.5
SWy–2-Ca, <1 μm	SEM	5	66.7	23.2	4.1	–	3.0	2.7	0.1	0.1
SWy–3-Ca, <1 μm*	SEM	5	68.8	21.1	3.6	–	2.7	2.5	0.1	0.0

Results normalized to 100% and without hydroxyls and water. Natl = natural state.
*Analyses including SiO_2 accessories. A linear correlation plot of the TEM-EDX compositions *vs* the XRD and SEM compositions produced a 1:1 curved with an R^2 of 0.99 (see Supplementary material, Table S2).

High-resolution imaging of the (001) basal lattices after inverse fast Fourier transformation (FFT) confirmed the 1.2 nm spacing and the tetrahedral and octahedral sheets as well as the interlayer spaces (Fig. 7d).

The mineral cristobalite, present in the <1 μm fraction of the SWy-3 sample, was identified in TEM images and avoided in EDX measurements. These occurred as small, commonly 20–30 nm in diameter, rounded or square-shaped crystals (Fig. 8a) to larger more irregularly shaped grains that contained twin bands with 60 or 120° angles between them (Fig. 8b). Some cristobalite crystals showed patchy shadows and enhanced contrast, probably reflecting lattice distortion. The most prominent lattice fringes were 0.40 nm thick which represent (101) planes. FFTs of the images produced tetragonal crystallographic patterns indicative of α-cristobalite defined by distinct diffraction spots (small inset images in Fig. 8). Some weak streaking of diffraction spots (marked by white arrows) indicated that minor disordering occurred along selected (hkl) planes. Inverse FFT images showed lattice structures (upper right inset in Fig. 8a) very similar to the simulated (010) projection for α-cristobalite (Elzea and Rice, 1996).

Crystallite thickness distributions

The thickness of the nanometer-thin crystallites was determined perpendicular to the crystallographic c-direction. These were obtained from the TEM images by measuring the defect-free distance following the procedure of Warr and Nieto (1998). All crystallite thickness distributions of the three SWy reference materials showed similar sizes mostly ranging between 2 and 25 nm (Fig. 9). The mean crystallite thickness was 7 nm and the most frequent number of layers was 2–6. The three samples also produced similar crystallite size distributions, with SWy-1 and SWy-2 having close to identical shapes. The SWy-3 sample indicated a slightly lower abundance of crystallites with thicknesses of 5–10 nm. The occurrence of occasional crystallites >25 nm in all samples may reflect the difficulty of recognizing layer discontinuities or layer terminations from 2-D images. If plotted on a logarithmic scale, the distributions appeared to have shapes that were close to lognormal (plots shown in the Supplementary material, Table S2).

Montmorillonite composition and layer-charge distributions

The mean wt.% montmorillonite oxide compositions of the three SWy bentonite reference materials in the natural state were chemically very similar (Fig. 1; Table 2). The SiO_2 content was 66.2–66.7 wt.% and the Al_2O_3 content was 23.8–24.4 wt.%. SWy-1 and SWy-2 also contained very similar amounts of Fe_2O_3 of 4.4 and 4.3 wt.%, respectively, whereas SWy-3 had a smaller content of 3.9 wt.%. This pattern was comparable to the MgO content whereby the SWy-3 sample was smaller (3.3 wt.%) than the other samples (3.6 and 3.5 wt.%) probably due to the greater SiO_2 content of this material. In terms of cations unique to the interlayer, CaO was consistent between the samples with a value of 0.6 wt.% as was K_2O with a range of ~0.2 to ~0.3 wt.%. The most variable was the Na_2O concentration, greatest in SWy-1 at ~1.3 wt.%, smallest in the SWy-2 at ~0.8 wt.%, and with an intermediate value of ~1.1 wt.% in SWy-1. Plotted on a ternary graph of SiO_2 *vs* $CaO+Na_2O+K_2O$ *vs* $Al_2O_2+Fe_2O_3+MgO$, the three points representing the SWy series plotted in the cluster of published compositions of grain size fractions <2 μm, 0.5–1 μm, 0.2–0.5 μm, and <0.1 μm (Fig. 1).

The composition of Ca-exchanged montmorillonites of the SWy series showed successful replacement of most of the Na^+ and K^+ with Ca^{2+} ions (Table 2) with only small amounts of Na_2O (~0.1 to 0.3 wt.%) and K_2O remaining (~0.1 wt.%). The Ca-exchanged montmorillonites also exhibited a consistent decrease in MgO by 0.3–0.6 wt.%. This was attributable to the exchange of the Mg^{2+} in the interlayer sites by Ca^{2+} ions. The total amount of CaO following the

https://doi.org/10.1017/cmn.2024.20 Published online by Cambridge University Press

Table 3. Reported stoichiometric formula (per $O_{10}(OH)_2$) for montmorillonites of the SWy sample series

			Si^{4+}	$^{IV}Al^{3+}$	$^{VI}Al^{3+}$	Fe^{3+}	Mg^{2+}	Na^{+}	Mg^{2+}	K^{+}	Ca^{2+}			
Sample	Method	*n*	Tetrahedral		Octahedral			Interlayer				TC	OC	TLC
SWy–1-K, <0.1 μm[a]	Not stated	1	3.90	0.10	1.53	0.22	0.26	0.02	–	0.30	–	−0.10	−0.24	−0.34
SWy–1-Ca, <2 μm[b,§]	Not stated	1	3.83	0.17	1.54	0.22	0.27	–	–	–	–	−0.17	−0.20	−0.37
SWy–1-Na, <0.5 μm[c]	XRF and AAS	1	3.93	0.07	1.52	0.21	0.27	0.35	–	0.00	–	−0.07	−0.26	−0.33
SWy–1-Na[d,*]	ICP-OES+EM	1	3.87	0.13	1.54	0.21	0.23	0.35	–	–	–	−0.13	−0.29	−0.42
SWy–1, <1 μm[e]	TEM-EDX	1	3.94	0.06	1.55	0.20	0.25	0.07	–	0.04	0.02	− 0.06	−0.28	−0.34
SWy–1[f,*]	Not stated	1	3.96	0.04	1.53	0.20	0.25	–	–	–	–	−0.04	−0.30	−0.34
SWy–2-Na[d,*]	ICP-OES+EM	1	3.88	0.12	1.55	0.23	0.25	0.37	–	–	–	−0.12	−0.19	−0.31
SWy–2, <2 μm[g]	AAS-FES	4	3.88	0.12	1.53	0.21	0.26	0.18	0.01	0.02	0.08	−0.12	−0.26	−0.38
SWy–2[h]	EM	–	3.95	0.05	1.56	0.21	0.23	0.14	–	0.01	0.05	−0.05	−0.23	−0.28
SWy–2-Na[i]	Not stated	1	3.88	0.12	1.54	0.23	0.24	0.31	–	–	0.01	−0.12	−0.21	−0.33
SWy–2, <0.2 μm[j]	XRF	1	3.79	0.21	1.53	0.23	0.32	–	–	–	–	−0.21	−0.24	−0.45
SWy–2-Na, <2 μm[k]	Not stated	1	3.95	0.05	1.53	0.21	0.29	0.34	–	–	–	−0.05	−0.20	−0.25
SWy–2-, <0.1 μm[l]	Not stated	1	3.88	0.12	1.53	0.23	0.24	–	–	–	–	−0.12	−0.24	−0.36
SWy–3[m]	STEM-EDX	46	3.93	0.07	1.57	0.20	0.23	0.13	0.02	0.05	0.04	−0.07	−0.23	−0.30
SWy–3-Ca[m]	STEM-EDX	31	3.94	0.06	1.58	0.20	0.23	–	–	–	0.14	−0.06	−0.23	−0.29
SWy–1-, <1 μm[‡]	TEM-EDX	151	3.90	0.10	1.56	0.19	0.27	0.12	0.04	0.02	0.04	−0.10	−0.21	−0.30
SWy–2-, <1 μm[‡]	TEM-EDX	154	3.89	0.11	1.58	0.19	0.26	0.09	0.04	0.02	0.04	−0.11	−0.16	−0.27
SWy–3-, <1 μm[‡]	TEM-EDX	149	3.92	0.08	1.60	0.17	0.26	0.14	0.02	0.02	0.04	−0.08	−0.19	−0.27

TC = tetrahedral charge, OC = octahedral charge, TLC = total layer charge
*Grain-size fraction not stated
[§]Adjusted for excess SiO_2 from quartz or cristobalite
AAS-FES = atomic absorption spectroscopy-flame emission spectroscopy, EM = electron microprobe, ICP-OES = inductively coupled plasma atomic emission spectroscopy
[a]Whitney and Northrop (1988)
[b]Madejová et al. (1994)
[c]McKinley et al. (1995)
[d]Vantelon et al. (2001)
[e]Duong et al. (2005)
[f]Czímerová et al. (2006)
[g]Mermut and Cano (2001)
[h]Lantenois et al. (2005)
[i]Zviagina et al. (2004)
[j]Steudel et al (2009)
[k]Le Forestier et al. (2010)
[l]Kuligiewicz and Derkowski (2017)
[m]Garcıa-Romero et al. (2021)
[‡]This study (with no cation exchange)

cation exchange treatment reached 1.8–2.1 wt.%. All other elemental oxides (SiO_2, Al_2O_3, and Fe_2O_3) produced very similar values as measured in the non-exchanged sample material (Table 2).

Calculation of the stoichiometric formulae for the Ca-saturated SWy montmorillonite (Tables 3 and 4) resulted in the number of octahedral cations ranging between 2.02 and 2.03 per $O_{10}(OH)_2$. This was very close to an ideal dioctahedral structure. When fixing the octahedral sums of the natural SWy samples to the same values, the excess Mg^{2+} allocated to the interlayers was 0.04 per $O_{10}(OH)_2$ for SWy-1 and SWy-2, and 0.02 per $O_{10}(OH)_2$ for SWy-3. As expected, the natural interlayer cation content was dominated by Na^{+} with values of 0.12 per $O_{10}(OH)_2$ for SWy-1, 0.09 per $O_{10}(OH)_2$ for SWy-2 and 0.14 per $O_{10}(OH)_2$ for SWy-3. Ca^{2+} was present in a similar amount to that of Mg^{2+} with 0.04 per $O_{10}(OH)_2$ in all three samples. Only a small concentration of 0.02 per $O_{10}(OH)_2$ K^{+} occurred in the non-cation exchanged montmorillonites.

Based on the amount of tetrahedrally exchanged Si^{4+} by Al^{3+} determined from both Ca-exchanged and non-exchanged montmorillonites, the mean tetrahedral charge was determined to be –0.09 per $O_{10}(OH)_2$ for SWy-1 (n = 175), –0.11 per $O_{10}(OH)_2$ for SWy-2 (n = 180) and –0.08 per $O_{10}(OH)_2$ for SWy-3 (n = 173). The corresponding octahedral charges were –0.21 per $O_{10}(OH)_2$ for SWy-1, –0.17 per $O_{10}(OH)_2$ for SWy-2 and –0.18 per $O_{10}(OH)_2$ for SWy-3, which then yielded a total layer charge of –0.30, –0.28, and –0.26 per $O_{10}(OH)_2$, respectively (Table 4). These averaged values had standard deviations (σ_1) typically in the range of 0.01–0.02 per $O_{10}(OH)_2$.

The montmorillonite layer charge distributions of the SWy-series also revealed some differences between the samples (Fig. 10). SWy-1 produced the most heterogeneous distribution in tetrahedral charge with a broad range from –0.04 to –0.15 per $O_{10}(OH)_2$ (Fig. 10a). This is in contrast to the narrower distribution of octahedral charges that largely ranged from –0.16 to –0.22 per

https://doi.org/10.1017/cmn.2024.20 Published online by Cambridge University Press

Table 4. Stoichiometric formula (per $O_{10}(OH)_2$) for montmorillonites of the SWy sample series determined in this study

			Si^{4+}	$^{IV}Al^{3+}$	$^{VI}Al^{3+}$	Fe^{3+}	Mg^{2+}	ΣOct	Na^{+}	Mg^{2+}	K^{+}	Ca^{2+}	TC	OC	TLC
Sample	Method	*n*	Tetrahedral		Octahedral				Interlayer				Charge		
SWy–1-Ca	TEM-EDX	24	3.91	0.09	1.57	0.19	0.26	2.02	<0.01	0.00	0.00	0.13	−0.09	−0.20	−0.28
STDEV (σ_1)			0.01	0.01	0.01	0.01	0.01	0.01	0.01	0.00	0.00	0.01	0.01	0.02	0.02
SWy–1-Natl	TEM-EDX	151	3.90	0.10	1.56	0.19	0.27	2.02	0.12	0.04	0.02	0.04	−0.10	−0.21	−0.30
STDEV (σ_1)			0.02	0.02	0.01	0.01	0.01	0.01	0.03	0.01	0.01	0.01	0.02	0.01	0.02
SWy–1, all data	TEM-EDX	175	–	–	–	–	–	–	–	–	–	–	−0.09	−0.21	−0.30
STDEV (σ_1)			–	–	–	–	–	–	–	–	–	–	0.00	0.01	0.02
SWy–2-Ca	TEM-EDX	26	3.89	0.11	1.57	0.19	0.28	2.03	0.03	0.00	0.01	0.13	−0.11	−0.18	−0.29
STDEV (σ_1)			0.02	0.02	0.01	0.01	0.01	0.02	0.01	0.00	0.00	0.01	0.02	0.02	0.02
SWy–2-Natl	TEM-EDX	154	3.89	0.11	1.58	0.19	0.26	2.03	0.09	0.04	0.02	0.04	−0.11	−0.16	−0.27
STDEV (σ_1)			0.02	0.02	0.02	0.01	0.02	0.02	0.03	0.02	0.01	0.01	0.02	0.02	0.02
SWy–2, all data	TEM-EDX	180	–	–	–	–	–	–	–	–	–	–	−0.11	−0.17	−0.28
STDEV (σ_1)			–	–	–	–	–	–	–	–	–	–	0.02	0.02	0.02
SWy–3-Ca	TEM-EDX	24	3.92	0.08	1.60	0.17	0.26	2.03	0.02	0.00	0.01	0.11	−0.08	−0.17	−0.25
STDEV (σ_1)			0.02	0.02	0.01	0.01	0.01	0.01	0.01	0.00	0.01	0.01	0.02	0.02	0.01
SWy–3-Natl	TEM-EDX	149	3.92	0.08	1.59	0.17	0.27	2.03	0.14	0.02	0.02	0.04	−0.08	−0.19	−0.27
STDEV (σ_1)			0.02	0.02	0.01	0.01	0.01	0.00	0.01	0.01	0.01	0.01	0.02	0.01	0.02
SWy–3, all data	TEM-EDX	173	–	–	–	–	–	–	–	–	–	–	−0.08	−0.18	−0.26
STDEV (σ_1)			–	–	–	–	–	–	–	–	–	–	0.02	0.01	0.02
SWy-Ca, all data	TEM-EDX	74	3.91	0.09	1.58	0.18	0.26	2.03	0.02	0.00	0.01	0.12	−0.09	−0.18	−0.28
STDEV (σ_1)			0.02	0.02	0.02	0.01	0.01	0.01	0.01	0.00	0.01	0.01	0.03	0.03	0.03
SWy-Natl, all data	TEM-EDX	454	3.91	0.09	1.57	0.19	0.27	2.03	0.12	0.03	0.02	0.04	−0.09	−0.19	−0.28
STDEV (σ_1)			0.02	0.02	0.02	0.01	0.01	0.01	0.03	0.02	0.01	0.01	0.02	0.02	0.03
SWy, all data	TEM-EDX	528	–	–	–	–	–	–	–	–	–	–	−0.09	−0.19	−0.28
STDEV (σ_1)			–	–	–	–	–	–	–	–	–	–	0.02	0.02	0.03

Natl = natural state, TC = tetrahedral charge, OC = octahedral charge, TLC = total layer charge.

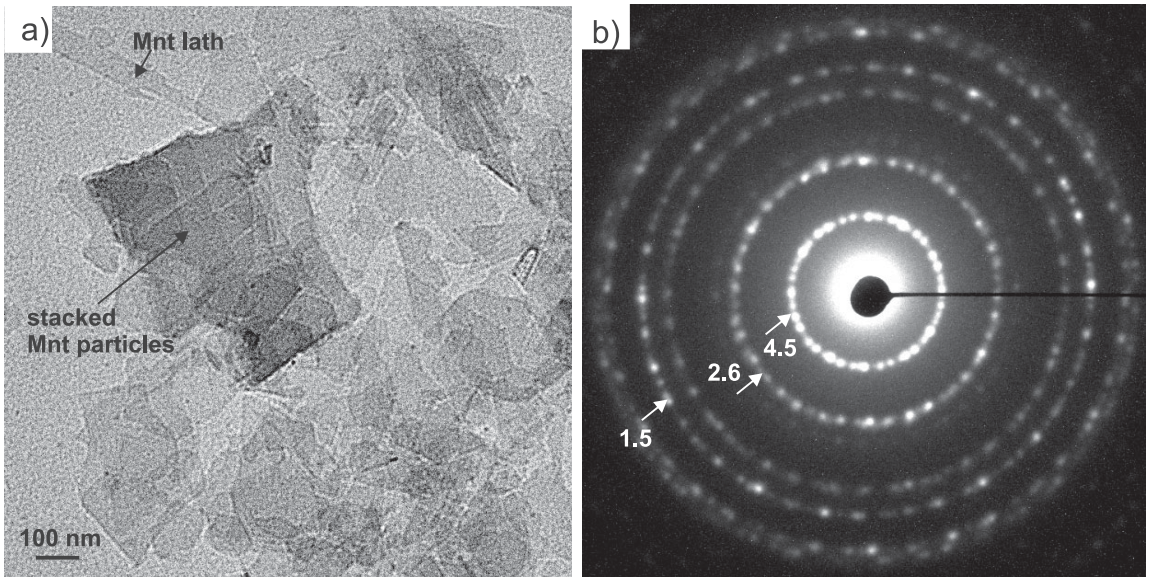

Figure 6. (a) TEM images of stacked montmorillonite particles with some occasional lath-shaped crystals (SWy-1 natural). (b) Selected area electron diffraction of stacked montmorillonite particles. Mnt = montmorillonite. d-values and Miller indices of the marked diffraction rings are 4.5 Å (020) (110), 2.6 Å (130) (200), and 1.5 Å (060) (330).

https://doi.org/10.1017/cmn.2024.20 Published online by Cambridge University Press

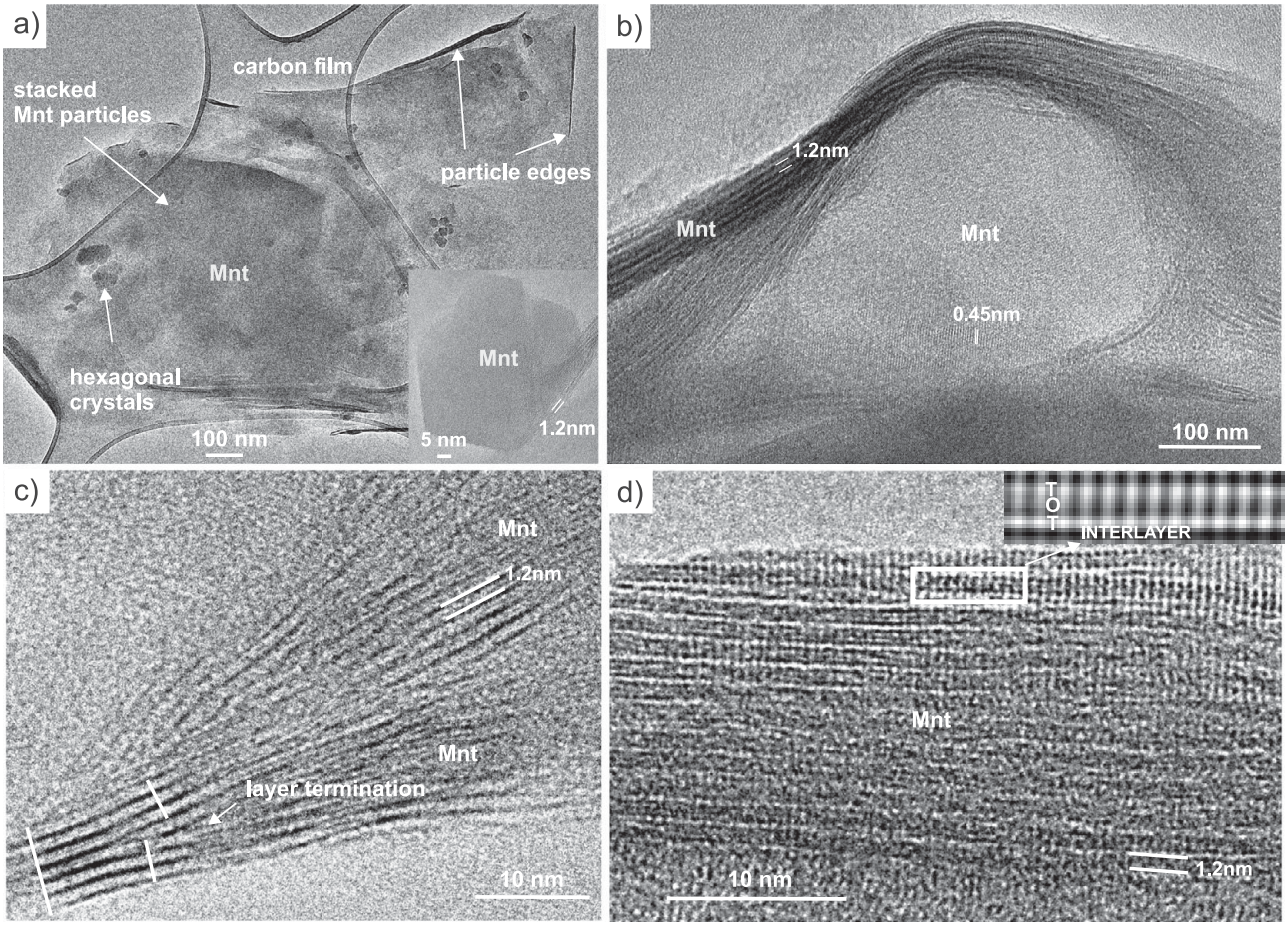

Figure 7. TEM images of montmorillonite particles (SWy-3 natural). (a) ~1 μm^2 aggregate of particles used for TEM-EDX measurements located over a hole in the lacey carbon film. The smaller hexagonal particles represent small <100 nm crystallites of montmorillonite (bottom right, inset). (b) Lattice fringes of particles stacked with (001) basal spacings of ~1.2 nm located around a flat sub-spherical montmorillonite with (020) cross fringes of 0.45 nm. (c) High-resolution lattice fringe images of (001) basal spacing with thicknesses of ~1.2 nm. The white lines mark the thickness of crystallites that are separated by layer terminations and low-angle discontinuities. (d) High-resolution image of the (001) basal spacing with an inset improved by inverse fast Fourier transformation to show the location of the tetrahedral (T), octahedral (O), and interlayer sheets.

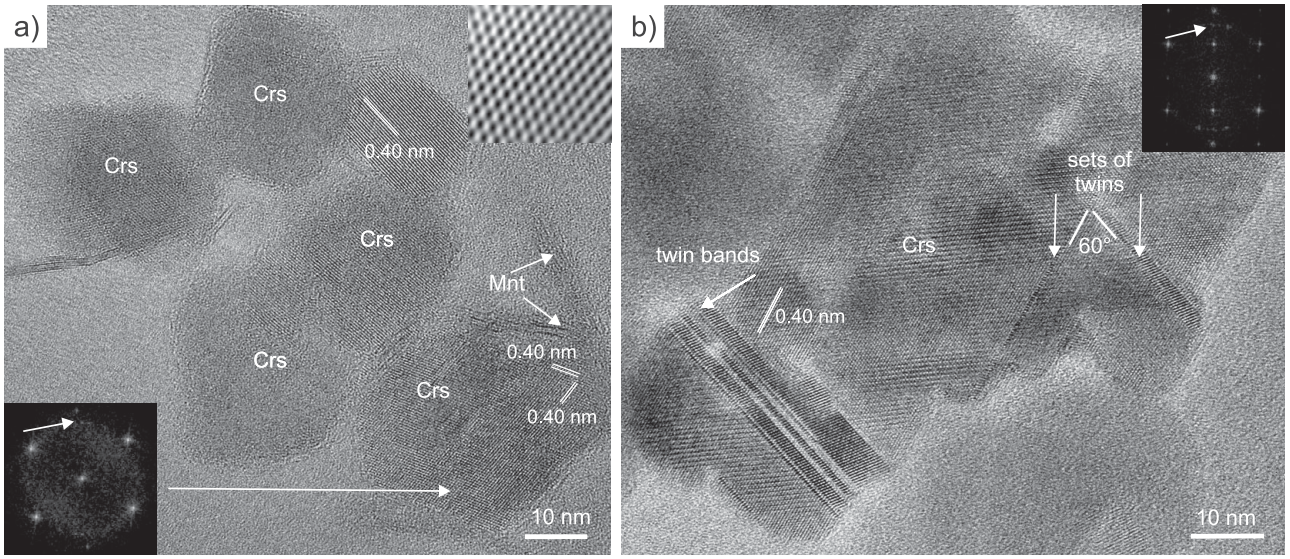

Figure 8. (a) TEM image of nanosized α-cristobalite (Crs) crystals (SWy-3 natural). Prominent lattice fringes occur with a thickness of 0.40 nm (101). A fast Fourier transformation (FFT) of the bottom right grain reveals the tetragonal symmetry of the α-cristobalite (bottom left) as does the inverse FFT (top right). (b) An irregular cristobalite grain showing a characteristic high contrast and twin sets marked by bands at 60° to each other. Prominent lattice fringes occur with a thickness of 0.40 nm (101). The arrows in the FFT insets indicate some diffuse ring structure suggestive of some minor crystal disorder.

https://doi.org/10.1017/cmn.2024.20 Published online by Cambridge University Press

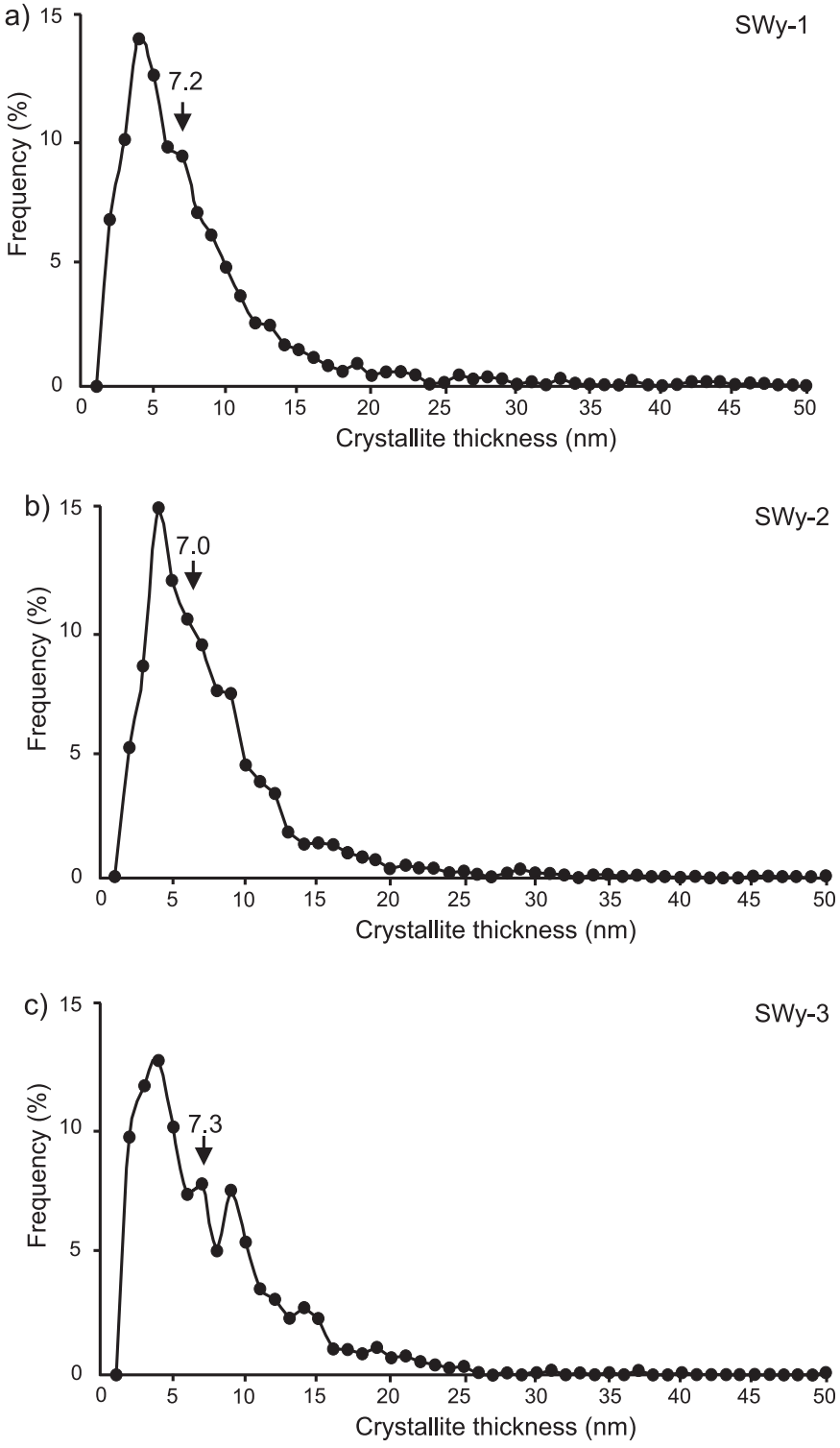

Figure 9. Montmorillonite crystallite thickness distributions for reference materials: (a) SWy-1, (b) SWy-2, and (c) SWy-3. The mean values are marked with arrows, which are 7.2 nm for SWy-1 (*n*=1284), 7.0 nm for SWy-2 (*n*=1232), and 7.3 nm for SWy-3 (*n*=1164).

$O_{10}(OH)_2$. The resulting broad range of the total layer charge in this sample (–0.23 to –0.34 per $O_{10}(OH)_2$) was attributable to compositional heterogeneities in the Si^{4+} and Al^{3+} content in the tetrahedral sheet (Fig. 11a). The reverse was the case for the SWy-2 sample, with a broad bi-modal charge distribution recognized in the octahedral sheet, which was also evident in the total layer charge (Fig. 10b). This heterogeneity corresponded mostly to the exchange of Al^{3+} by Mg^{2+}, whereby the higher negative charges were caused by the increased Mg^{2+} content in the octahedral sheets at the expense of trivalent ions (Fig. 11b). In contrast, the octahedral Fe^{3+} remained relatively constant with changes in octahedral charge. In the case of SWy-2, there appeared to be two populations in terms of the amount

https://doi.org/10.1017/cmn.2024.20 Published online by Cambridge University Press

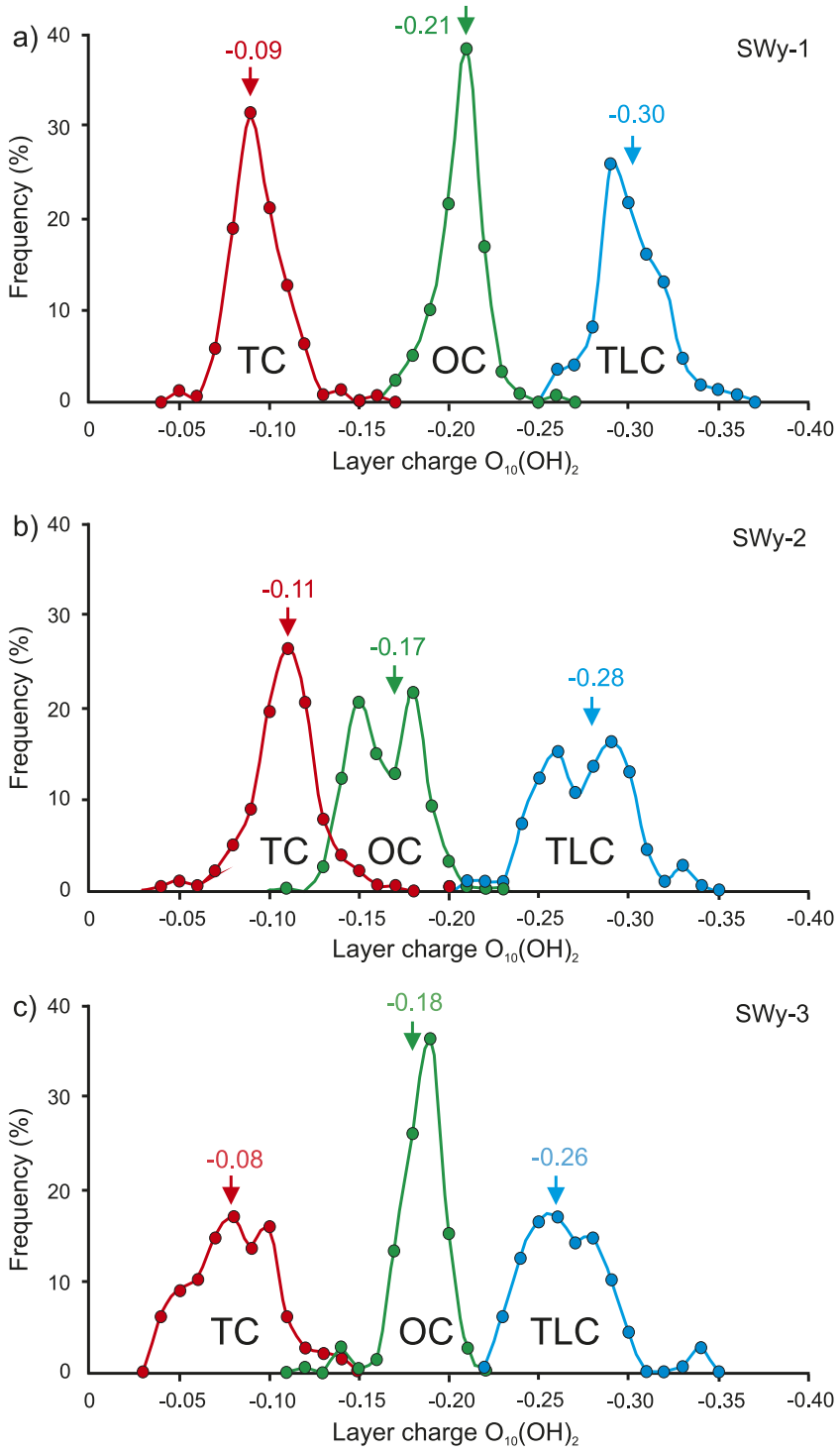

Figure 10. Montmorillonite layer charge distributions for (a) SWy-1, (b) SWy-2, and (c) SWy-3. TC = tetrahedral charge; OC = octahedral charge; TLC = total layer charge.

of octahedral and interlayer Mg^{2+} present: one population responsible for the greater octahedral charges contained higher Al^{3+} and lower Mg^{2+} with relatively more Mg^{2+} in the interlayer. The other population responsible for the lower octahedral charges contained lower Al^{3+} and higher Mg^{2+} with less Mg^{2+} in the interlayer (Fig. 11c). Such heterogeneities in tetrahedral or octahedral substitutions were less evident in SWy-3, where the more distinct distributions had smaller degrees of charge variation (Fig. 10c).

Discussion

Obtaining precise and accurate montmorillonite compositions by TEM-EDX analyses

Several analytical problems limit the precision and accuracy of TEM-based EDX measurements of clay mineral composition and require solutions before reliable elemental quantifications can be made. These are (i) acquiring adequate counting statistics to enable precise measurements, (ii) avoiding any beam damage of the clay

https://doi.org/10.1017/cmn.2024.20 Published online by Cambridge University Press

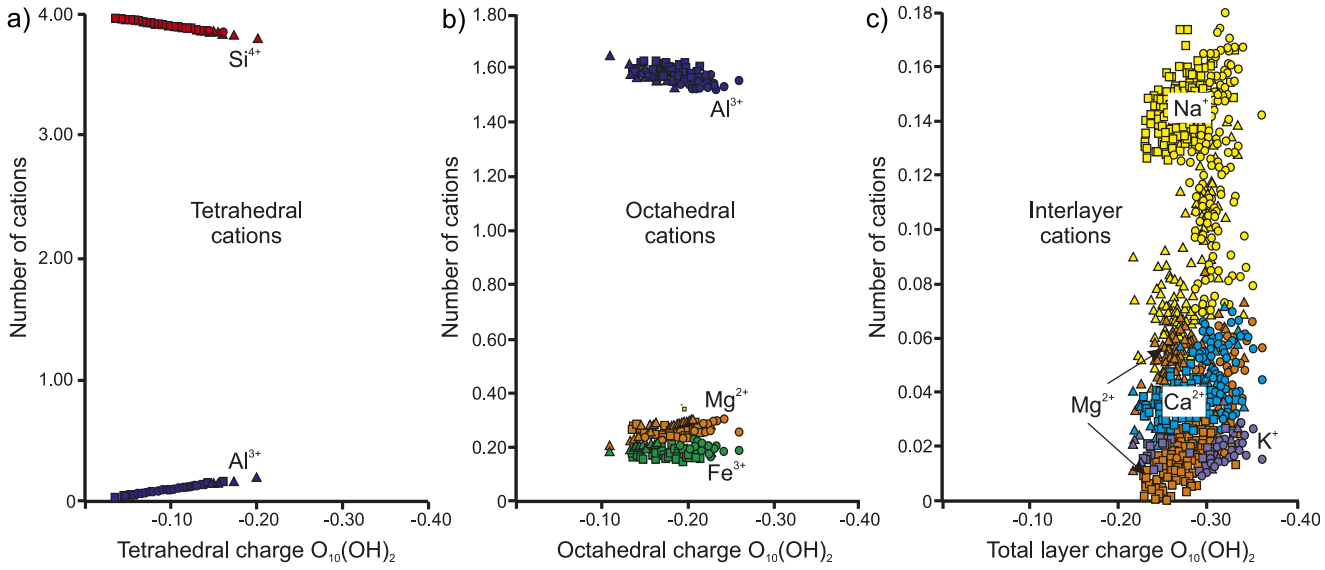

Figure 11. Number of cations per formula unit (per $O_{10}(OH)_2$) *vs* charge properties of the Wyoming montmorillonite. (a) Tetrahedral cations (Si^{4+} and Al^{3+}) *vs* tetrahedral charge, which are mathematically fixed to four cations; (b) octahedral cations (Al^{3+}, Mg^{2+}, Fe^{3+}) *vs* octahedral charge; (c) interlayer cations (Na^+, Ca^{2+}, Mg^{2+}, K^+) *vs* total layer charge. Symbols: circles = SWy-1, triangles = SWy-2, and squares = SWy-3. Color code for elements as in Fig.5.

minerals during data acquisition, and (iii) calibrating the k-values used for the TEM instrument based on standards that apply to clay minerals and are not affected by the problems (i) and (ii). Despite montmorillonite being particularly challenging due to commonly reported low counts from the very thin particles and rapid beam damage, this study successfully overcame all three of the outlined problems by adopting the following procedure.

Firstly, high counts per second were attained by using the TEM mode where the electron beam is parallel and the intensities are 2- to 10-fold higher than those recorded by STEM, which uses a convergent beam. The time-dependent measurements with counting rates of 10,000–20,000 cps and low dead times (2–3%) were sufficient to precisely determine element concentrations after 20–50 s of area measurement (Fig. 3b,c). Such high intensities obtained from the thin montmorillonite particles were also possible due to the fast and sensitive 100 mm^2 SDD detector used, which acquires significantly more counts than the 10 or 30 mm^2 Si(Li)-detectors employed in many past studies (Ahn and Peacor, 1986; Nieto, 2002; Hüpers et al., 2019; Hoang-Minh et al., 2019; García-Romero et al., 2021).

Secondly, measuring in the TEM mode at 50,000× magnification and spot size 1, in combination with a low beam current of 101.7 μA, resulted in no detectable beam damage (Fig. 3). The absence of beam damage can be monitored easily by the constant levels of Si detected over the time of measurements, which otherwise increases if any cations migrate out of the electron beam. Beam damage effects could be observed at 100,000× magnification when analyzing the edge of some particles (Fig. 4). The lack of beam damage at 50,000× magnification with a beam current of 101.7 μA was also evident when measuring the composition of the KGa-1b and KGa-2 kaolinite standards, which represent minerals that are notorious for their rapid breakdown (Bergaya et al., 1993; Kogure and Inoue, 2005). TEM-EDX measurements of these samples showed no time-dependent changes in Al or Si, and no visible damage to the specimen during the 90 s of data acquisition.

Thirdly, the k-values were adjusted using appropriate pure phyllosilicate minerals of well-constrained composition determined by XRF. These minerals were prepared as small thin crystals (<1 μm fraction) to mimic the thickness of the montmorillonite particles of the SWy material. It was also important to select minerals with large concentrations of the element to be calibrated, i.e. kaolinite for Al, biotite for Fe, vermiculite for Mg, muscovite, phlogopite and biotite for K, and paragonite for Na. Due to the absence of a good Ca-rich phyllosilicate, epidote and prehnite were used to adjust the k-value of Ca. All k-values were manually adjusted to obtain the best possible 1:1 correlation (R^2=0.999) between TEM-EDX results and the XRF compositions (Fig. 5). After calibration, the accuracy of the TEM-EDX results using the separated <1 μm bentonite fractions were cross-checked by SEM-EDX measurements that were calibrated using an independent set of mineral standards (Podlech et al., 2021).

Based on this procedure of TEM-EDX measurement that provided high counting intensities and lacked beam damage-induced migration, along with manual calibration of the k-values using phyllosilicate standards, both accurate and precise composition analyses were obtained for montmorillonite particles of the SWy bentonites.

Comparison of the three Wyoming (SWy) reference materials

As the three Wyoming bentonite materials were collected from the same location in 1972, 1993, and 2018, and made available to the scientific community, the degree of homogeneity between the sources is of current interest. Based on our investigation, the materials are indeed very similar but some differences occur in terms of the clay's precise mineralogy and montmorillonite composition. These may partly reflect heterogeneities within the individual batches of source clay, an aspect that could not be investigated in this study. It is, however, considered more likely that the reported differences represent variations between the

https://doi.org/10.1017/cmn.2024.20 Published online by Cambridge University Press

different collections of each source clay, as resampling precisely the same material was not possible from year to year.

Based on the general mineralogy of the three source batches investigated by XRD and TEM, all bentonites analyzed in their natural form were dominated by Na-montmorillonite and contained traces of muscovite and quartz in the <1 μm size fraction (Fig. 2). Whereas calcite was detected only in the <1 μm size fraction of SWy-3, this mineral has been reported to be present in the coarse grain-sized fractions of SWy-1 and SWy-2 (Koster van Groos and Guggenheim, 1984; Vogt et al., 2002). Other minerals previously identified, such as feldspars, pyroxenes, gypsum, kaolinite or chlorite, were not detected in the fine fractions used in this study. One distinct difference in the mineralogy was observed in SWy-3 with the presence of 5.3 wt.% cristobalite (Fig. 2a). This mineral was identified in more than one batch of SWy-3 obtained from the Source Clays Repository of The Clay Minerals Society and is considered to be representative of this material. This mineral was not detected in SWy-1 or SWy-2, confirming the result of Hillier and Lumsdon (2008) based on Na-hydroxide treatment of the SWy-1 sample that indicated no dissolvable SiO_2 to be present.

The small crystals of cristobalite imaged by TEM in SWy-3 had tabular to irregular crystal shapes, contained characteristic twin sets, areas of lattice distortion, and a tetragonal crystal system indicative of α-cristobalite (Fig. 8). This polymorph is known to form during the cooling of rhyolitic lava domes by vapour-phase mineralization and devitrification of the volcanic groundmass, whereby the high-temperature polymorph of β-cristobalite converts to a lower temperature α-cristobalite (Damby et al., 2014). Although not often reported in bentonites, it is a common mineral in young ash deposits (Hillier and Lumsdon, 2008). The characteristics of the cristobalite described in SWy-3 appeared to be different from the opal lattice features described in a Wyoming bentonite sample collected from the same location (Elzea and Rice, 1996) with no indication of any tridymite layers in the crystals studied that would be suggestive of an opaline phase. Due to the lack of rigorous testing, however, we cannot rule out the presence of some opal in the SWy-3 sample.

All montmorillonites of the SWy sample series showed the same characteristics in TEM images. The <1 μm particles represent aggregates of small montmorillonite crystallites that were typically tens to hundreds of nanometers in size. These were turbostratically stacked randomly on top of each other with individual crystallites having curved or straight edges and displaying lath or hexagonal crystal shapes (Figs 6a and 7a). The crystallites were observed to be separated by numerous low-angle boundaries and edge dislocations that probably formed by the non-parallel aggregation of meso-crystals during crystallization (García-Romero and Suárez, 2018) and likely developed by growth associated with dissolution of the glass-rich phases present in rhyolitic parent ash. The conversion to montmorillonite has been suggested to have begun as the Wyoming parent ash fell into a shallow sea or lagoonal environment (Moll, 2001). The basal montmorillonite (001) lattice thickness resolved at higher resolution was typically ~0.12 nm for both natural samples prepared in ethanol (SWy-Natl) and Ca-saturated samples prepared in water (SWy-Ca). This indicates that an air-dried mono-layer of ethanol (0.13 nm; Cui et al., 2023) or a monolayer of water (0.123–0.127 nm; Ferrage et al., 2005) was the stable configuration in the vacuum of the TEM during the study.

The lognormal montmorillonite crystallite size distributions (Supplementary material, Table S2) indicate initial nucleation and growth occurred probably by surface spreading without continuous nucleation. The observation that smaller nanosized crystallites grew on larger aggregates does, however, imply that nucleation may not have been a singular event (Fig. 7a). The high-angle crystallite packets commonly located around the margin of aggregates or single crystallite particles (Fig. 7b) as well as around the margin of cristobalite crystals (Fig. 8a) are also suggested to reflect nucleation and growth in an environment lacking strong deviatoric stress and within a loosely compacted precursor ash deposit. The resultant crystallite size distributions were also remarkably similar with all three samples having an average thickness of 7–7.3 nm (Fig. 9) and are suggestive of equivalent crystal growth conditions (Fig. 10).

Despite the similar appearance of the montmorillonite particles in SWy-1, SWy-2, and SWy-3, there were some distinct differences in compositions and layer charge distributions between materials. These differences are not significantly large if compared with previously published data when similar grain sizes are compared, as displayed on a ternary plot of SiO_2 *vs* $CaO+Na_2O+K_2O$ *vs* $Al_2O_3+Fe_2O_3+MgO$ (Fig. 1).

Layer charge properties of the three Wyoming (SWy) montmorillonites

One interesting feature was the bi-modal layer charge distribution of the SWy-2 sample, which resulted from the bimodal octahedral charge distribution linked to a group of montmorillonite particles with greater charges, which were characterized by more substitution of Al^{3+} by Mg^{2+} and reduced interlayer Mg^{2+} (Fig. 11). A second group of lower charged particles had smaller amounts of substitution of Al^{3+} by Mg^{2+} and an increased interlayer content of Mg^{2+}. As this pattern was only evident in the SWy-2 sample and not present in SWy-1 and SWy-3, it is considered unlikely to result from the assumptions made in applying the SF method. The cause of the two populations of layer charges resulting from metal substitutions in octahedral sites remains uncertain. One possibility is that it resulted from small-scale compositional variations in the original ash, whereby variations in the mobility of Al^{3+} limited the amount of substitution that occurred and the way that Mg^{2+} was partitioned between octahedral and interlayer sites.

To verify that the bi-modal distribution was not an artefact of the TEM-EDX method, the accuracy of the total layer charge distribution was checked against available data using the well-established but time-consuming AAM of Lagaly and Weiss (1975). Very similar results were obtained when plotting the AAM results of the SWy-2 sample determined by Hofmann (2003) against the total layer charge distribution determined on multiple crystallite stacks in this study by TEM-EDX and the SF method (Fig. 12). Both independent methods produced a bi-modal distribution and a mean charge of –0.28 $O_{10}(OH_2)$ for this sample. The slightly broader distribution of charges measured using the AAM compared with the TEM-EDX results was probably because the bulk powder was used for the AAM, compared with the <1 μm fraction for the TEM-EDX-based results. Despite the very good correspondence of the total layer charge distribution determined by the two methods, this relationship is likely only to apply to low layer charge smectite that contain minimal amounts of fixed cations in the interlayer (Christidis, 2008; Kaufhold et al., 2011; Christidis et al., 2023).

When plotting the number of cations (per $O_{10}(OH)_2$) *vs* the tetrahedral, octahedral and total layer charges, the patterns do reveal the substitution mechanisms that were responsible for the

https://doi.org/10.1017/cmn.2024.20 Published online by Cambridge University Press

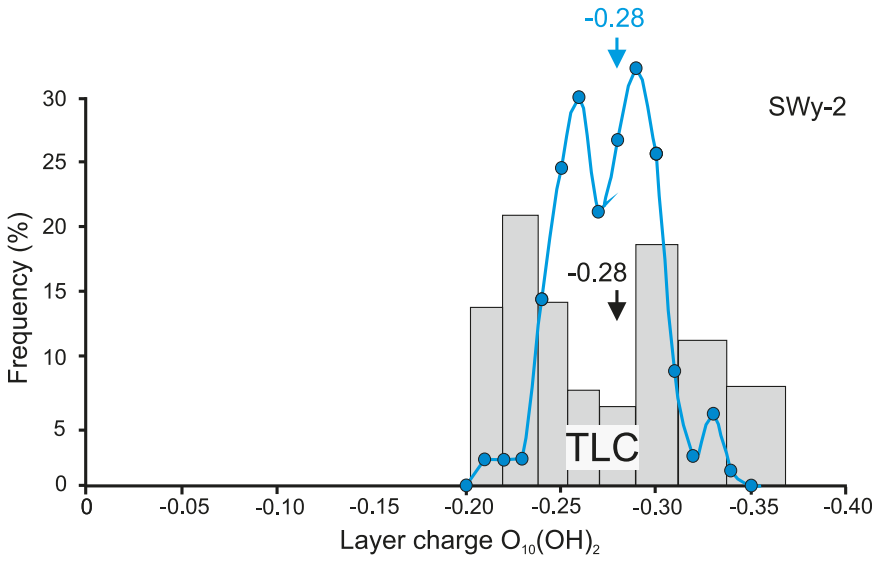

Figure 12. Comparison of the montmorillonite total layer charge (TLC) distributions for the <1 μm fraction of SWy-2 determined by TEM-EDX composition analyses (blue line) and the bulk powder fraction determined by the alkylammonium method of Lagaly (1972). The latter is shown in the form of a histogram plotted from the results of Hofmann (2003).

observed differences in the distribution of layer charge (Fig. 11). In addition to Si^{4+} substitution by Al^{3+} controlling tetrahedral charge and Al^{3+}substitution by Mg^{2+} as the main origin of the octahedral charges, the distribution of interlayer cations shows some other relevant features. The general increase in the interlayer content of many of the cations with increasing total layer charge is visible and appears to be achieved largely by an increase of interlayer Mg^{2+} and Na^{+} whereas the concentration of Ca^{2+} and K^{+} remained less variable (Fig. 11c).

The described differences in layer charges between the three samples are small when plotted on the ternary muscovite-celadonite-pyrophyllite charge plot (Fig. 13) of Newman and Brown (1987). Compared with published results, the TEM-EDX data represent some of the smallest layer charges measured for the

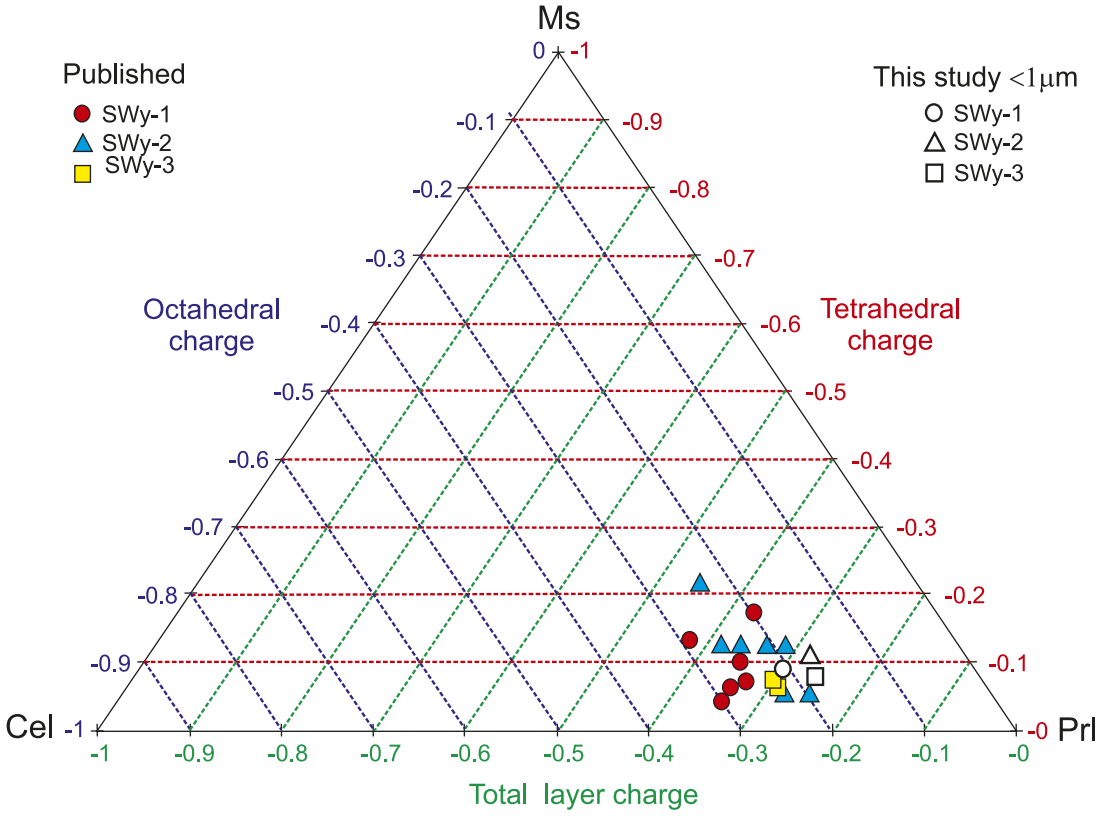

Figure 13. Triangle muscovite (Ms)–celadonite (Cel)–pyrophyllite (Prl) plot showing the mean charge properties (tetrahedral, octahedral, and total layer) of montmorillonite in the SWy-sample series (SWy-1, SWy-2, SWy-3). Plot modified from Newman and Brown (1987). IMA-approved mineral abbreviations after Warr (2020). The unit of layer charge is per $O_{10}(OH)_2$.

https://doi.org/10.1017/cmn.2024.20 Published online by Cambridge University Press

SWy series samples, showing low tetrahedral and octahedral charges characteristic of montmorillonite clay minerals. A beidellitic component to the montmorillonite composition, as suggested by Derkowski and Kuligiewicz (2017) was confirmed with an average of –0.09 per $O_{10}(OH)_2$ $^{IV}Al^{3+}$ being located in the tetrahedral sheet. Based on these composition constraints of 528 analyses, an improved average stoichiometric formula of the SWy-series can be written (Table 4): $(Na_{0.12}Ca_{0.04}Mg_{0.03}K_{0.02})(Si_{3.91}Al_{0.09})(Al_{1.57}Mg_{0.27}Fe_{0.19})_{2.03}$ $O_{10}(OH)_2 \cdot nH_2O$, whereby layer charge properties are –0.09±0.02 $O_{10}(OH)_2$ for the tetrahedral sheet, –0.19±0.02 $O_{10}(OH)_2$ for the octahedral sheet and –0.28±0.03 $O_{10}(OH)_2$ for the total interlayer.

Conclusions

Precise and accurate TEM-based EDX measurements of montmorillonite crystallites can be obtained as long as attention is given to acquiring adequate X-ray counts, avoiding beam damage-related ion migration and careful calibration of the k-values using appropriate pure phyllosilicate standards of constrained composition. Using this approach, an improved generalized structural formula for the SWy series montmorillonite can be determined along with new constraints on layer charge distributions. For the tetrahedral and octahedral sheets, the mean charges are –0.09±0.02 $O_{10}(OH)_2$ and –0.19±0.02 $O_{10}(OH)_2$, respectively. The total layer charge has a mean of –0.28±0.03 $O_{10}(OH)_2$ and a charge distribution consistent with the alkylammonium method determination for this low-charge smectite. Furthermore, only small differences in charge distributions exist between the three Wyoming bentonite collections, which are attributed to natural heterogeneities at the Crook County sample location. The SWy montmorillonite is a well-crystalline smectite that displays good hexagonal to lath-shaped crystallites with average thicknesses of 7 nm. The montmorillonite aggregates consisted of coalesced packets with numerous low-angle boundaries and edge dislocations that are suggested to have formed during heterogeneous crystal growth probably directly from glass-rich phases present in the rhyolitic parent ash. The SWy-3 sample also contains α-cristobalite, which is not common to bentonites, and could represent a useful reference material from this mineral if characterized in more detail.

Supplementary material. To view supplementary material for this article, please visit http://doi.org/10.1017/cmn.2024.20.

Author contribution. Conceptualization: Laurence N. Warr; Georg H. Grathoff Formal analysis: Laurence N. Warr; Balu R. Thombare, Rickwick Sudheer Kumar Investigation: Laurence N. Warr; Balu R. Thombare, Rickwick Sudheer Kumar Methodology: Laurence N. Warr; Balu R. Thombare, Rickwick Sudheer Kumar, Markus Peltz, Carolin PodlechProject administration: Laurence N. Warr, Georg H. Grathoff Visualization: Laurence N. Warr; Balu R. Thombare, Rickwick Sudheer Kumar Writing–original draft: Laurence N. Warr Writing–review & editing: All authors.

Acknowledgements. Reinhard Kleeberg (TU Bergakademie Freiberg) is thanked for providing some of the original SWy-1 material. We also thank Fernando Nieto, Arkadiusz Derkowski and an anonymous peer for reviewing this contribution.

Financial support. The JEOL 2100 Plus TEM microscope used in this study was financed by the Deutsche Forschungsgemeinschaft (DFG project number 428027021; https://gepris.dfg.de/gepris/projekt/428027021).

Competing interest. The authors declare none.

Data availability statement. The analytical data used in this paper is available in the Supplementary material. Additional results are available upon reasonable request.

References

Ahn, J.H., & Peacor, D.R. (1986). Transmission and analytical electron microscopy of the smectite-to-illite transition. *Clays and Clay Minerals*, *34*, 165–179. https://doi.org/10.1346/CCMN.1986.0340207

Ahn, J.H., Peacor, D.R., & Essene, E.J. (1986). Cation-diffusion-induced characteristic beam damage in transmission electron microscope images of mica. *Ultramicroscopy*, *19*, 375–381. https://doi.org/10.1016/0304-3991(86)90097-5

Bergaya, F., Dion, P., Alcover, J.-F., Clinard, C., & Tchoubar, D. (1993). TEM study of kaolinite thermal decomposition by controlled-rate thermal analysis. *Journal of Materials Science*, *31*, 5069–5075. https://doi.org/10.1007/BF00355907

Bishop, J.L., Murad, E., Madejova, J., Komadel, P., Wagner, U., & Scheinost, A.C. (1999). Visible, Mössbauer and infrared spectroscopy of dioctahedral smectites: structural analyses of the Fe-bearing smectites Sampor, SWy-1 and SWa-1. 11th International Clay Conference, pp. 413–419.

Bourdelle, F., Parra, T., Beyssac, O., Chopin. C., & Moreau, F. (2012). Ultrathin section preparation of phyllosilicates by focused ion beam milling for quantitative analysis by TEM-EDX. *Applied Clay Science*, *59–60*, 121–130. https://doi.org/10.1016/j.clay.2012.02.010

Byun, Y., Seo, C., Yun, T., Joo, Y., & Jo, H.Y. (2023). Prediction of Na- and Ca-montmorillonite contents and swelling properties of clay mixtures using Vis-NIR spectroscopy. *Geoderma*, *430*, 116294. https://doi.org/10.1016/j.geoderma.2022.116294

Chen, Q., Dwyer, C., Sheng, G., Zhu, C., Li, X., Zheng, C., & Zhu, Y. (2020). Imaging beam-sensitive materials by electron microscopy. *Advanced Materials*, *32*, 1907619. https://doi.org/10.1002/adma.201907619

Chipera, S.J., & Bish, D.L. (2001). Baseline studies of the Clay Minerals Society source clays: powder X-ray diffraction analyses. *Clays and Clay Minerals*, *49*, 398–409.

Christidis, G.E. (2006). Genesis and compositional heterogeneity of smectites. Part III: alteration of basic pyroclastic rocks. A case study from the Troodos ophiolite complex, Cyprus. *American Mineralogist*, *91*, 685–701.

Christidis, G.E. (2008). Validity of the structural formula method for layer charge determination of smectites: a re-evaluation of published data. *Applied Clay Science*, *42*, 1–7. https://doi.org/10.1016/j.clay.2008.02.002

Christidis, G.E., Blum, A.E., & Eberl, D.D. (2006). Influence of layer charge and charge distribution of smectites on the flow behaviour and swelling of bentonites. *Applied Clay Science*, *34*, 125–138. https://doi.org/10.1016/j.clay.2006.05.008

Christidis, G.E., Chryssikos, G.D., Derkowski, A., Dohrmann, R., Eberl D.D., Joussein, E., & Kaufhold, S. (2023). Methods for determination of the layer charge of smectites: a critical assessment of existing approaches. *Clays and Clay Minerals*, *71*, 25–53. https://doi.org/10.1007/s42860-023-00234-8

Cuadros, J., Nieto, F., & Wing-Dudek, T. (2009). Crystal-chemical changes of mixed-layer kaolinite-smectite with progressive kaolinization, as investigated by TEM-AEM and HRTEM. *Clays and Clay Minerals*, *57*, 742–750. https://doi.org/10.1346/CCMN.2009.0570607

Cui, R., Kumar, A., Nair, N., Yang, Y., & Sun, S. (2023). Molecular simulation study of montmorillonite in contact with ethanol. *Industrial & Engineering Chemistry Research*, *62*, 2978−2988. https://doi.org/10.1021/acs.iecr.2c03903

Cui, Y.-J. (2017). On the hydro-mechanical behaviour of MX80 bentonite-based materials. *Journal of Rock Mechanics and Geotechnical Engineering*, *9*, 565–574. https://doi.org/10.1016/j.jrmge.2016.09.003

Czímerová, A., Bujdák, J., & Dohrmann, R. (2006). Traditional and novel methods for estimating the layer charge of smectites. *Applied Clay Science*, *34*, 2–13. https://doi.org/10.1016/j.micromeso.2005.03.006

Damby, D.E., Damby, Llewellin, E.W., Horwell, C.J., Williamson, B.J., Najorka, J., Cressey, G., & Carpenter, M. (2014). The α–β phase transition in volcanic cristobalite. *Journal of Applied Crystallography*, *47*, 1205–1215. https://doi.org/10.1107/S160057671401070X

Derkowski, A., & Kuligiewicz, A. (2017). Tightly bound water in smectites. *American Mineralogist*, *102*, 1073–1090. https://doi.org/10.2138/am-2017-5918

Doebelin, N., & Kleeberg, R. (2015). Profex: a graphical user interface for the Rietveld refinement program BGMN. *Journal of Applied Crystallography*, *48*, 1573–1580. https://doi.org/10.1107/S1600576715014685

Duong, L., Bostrom, T., Kloprogge, T., & Frost, R. (2005). The distribution of Ga in Ga-pillared montmorillonites: a transmission electron microscopy and microanalysis study. *Microporous and Mesoporous Materials*, *82*, 165–172. https://doi.org/10.1016/j.micromeso.2005.03.006

Egerton, R.F., Li, P., & Malac, M. (2004). Radiation damage in the TEM and SEM. *Micron*, *35*, 399–409. https://doi.org/10.1016/j.micron.2004.02.003

Elzea, J.M., & Rice, S.B. (1996). TEM and X-ray diffraction evidence for cristobalite and tridymite stacking sequences in opal. *Clays and Clay Minerals*, *44*, 492–500. https://doi.org/10.1346/CCMN.1996.0440407

Elzea, J.M., Odom, I.E., & Miles, W.J. (1994). Distinguishing well-ordered opal-CT and opal-C from high-temperature cristobalite by X-ray diffraction. *Analytica Chimica Acta*, *286*, 107–116. https://doi.org/10.1016/0003-2670(94)80182-7

Emmerich, K., Wolters, F., Kahr, G., & Lagaly, G. (2009). Clay profiling: the classification of montmorillonites. *Clays and Clay Minerals*, *57*, 104–114. https://doi.org/10.1346/CCMN.2009.0570110

Ferrage, E., Lanson, B., Sakharov, B.A., & Drits, V.A. (2005). Investigation of smectite hydration properties by modeling experimental X-ray diffraction patterns: Part I. Montmorillonite hydration properties. *American Mineralogist*, *90*, 1358–1374. https://doi.org/10.2138/am.2005.1776

Finck, N., Schlegel, M.L., & Bauer, A. (2015). Structural iron in dioctahedral and trioctahedral smectites: a polarized XAS study. *Physics and Chemistry of Minerals*, *42*, 847–859. https://doi.org/10.1007/s00269-015-0768-3

García-Romero, E., & Suárez, M. (2018). A structure-based argument for non-classical crystal growth in natural clay minerals. *Mineralogical Magazine*, *82*, 171–180. https://doi.org/10.1180/minmag.2017.081.031

García-Romero, E., Lorenzo, A., García-Vicente, A., Morales, J., García-Rivas, J., & Suárez, M. (2021). On the structural formula of smectites: a review and new data on the influence of exchangeable cations. *Journal of Applied Crystallography*, *54*, 251–262. https://doi.org/10.1107/S1600576720016040

Hillier, S., & Lumsdon, D.G. (2008). Distinguishing opaline silica from cristobalite in bentonites: a practical procedure and perspective based on NaOH dissolution. *Clay Minerals*, *43*, 477–486. https://doi.org/10.1180/claymin.2008.043.3.11

Hoang-Minh, T., Kasbohm, J., Nguyen-Thanh, L., Nga, P.T., Lai, L.T., Duong, N. T., Thanh, N.D., Thuyet, N.T.M., Anh, D.D., Pusch, R., Knutsson, S., & Ferreiro Mählmann, R. (2019). Use of TEM-EDX for structural formula identification of clay minerals: a case study of Di Linh bentonite. *Vietnam. Journal of Applied Crystallography*, *52*, 133–147. https://doi.org/10.1107/S1600576718018162

Hofmann, H. (2003). Einfluss konzentrierter Salzlösungen auf die physiko-chemischen Eigenschaften quellfähiger tonminerale: Konsequenzen für den Einsatz von Bentonit als versatzmaterial in einem Endlager für schwach- und mittelradioaktive Abfälle in Salzformationen. Doctoral thesis, University of Heidelberg, 140 pp. https://archiv.ub.uni-heidelberg.de/volltextserver/3483/

Hüpers, A., Grathoff, G., Warr, L.N., Wemmer, K., Spinelli, G., & Underwood, M.B. (2019). Spatiotemporal characterization of smectite-to-illite diagenesis in the Nankai Trough accretionary prism revealed by samples from 3 km below seafloor. *Geochemistry, Geophysics, Geosystems*, *20*, 933–951. https://doi.org/10.1029/2018GC008015

Kaufhold, S., Dohrmann, R., Stucki, J.W., & Anastácio, A.S. (2011). Layer charge density of smectites – closing the gap between the structural formule method and the alkyl ammonium method. *Clays and Clay Minerals*, *59*, 200–211. https://doi.org/10.1346/CCMN.2011.0590208

Kogure, T. (2020). Visualization of clay minerals at the atomic scale. *Clay Minerals*, *55*, 203–218. https://doi.org/10.1180/clm.2020.27

Kogure, T., & Inoue, A. (2005). Determination of defect structures in kaolin minerals by high-resolution transmission electron microscopy (HRTEM). *American Mineralogist*, *90*, 85–89. https://doi.org/10.2138/am.2005.1603

Koster von Groos, A.F., & Guggenheim, S. (1984). The effect of pressure on the dehydration reaction of interlayer water in Na-montmorillonite (SWy-1). *American Mineralogist*, *69*, 872–879. https://doi.org/10.1346/CMS-WLS-3.3

Kuligiewicz, A., & Derkowski, A.D. (2017). Tightly bound water in smectites. *American Mineralogist*, *102*, 1073–1090. http://doi.org/10.2138/am-2017-5918

Lagaly, G. (1994). Layer charge determination by alkylammonium ions. *In A.R. Mermut (ed),* Layer Charge Characteristics of 2:1 Silicate Clay Minerals (pp. 2–46). CMS Workshop lectures, vol. *6*. The Clay Minerals Society, Boulder, CO, USA.

Lagaly, G., & Weiss, A. (1975). The layer charge of smectitic layer silicates. Proceedings of the International Clay Conference, Mexico, pp. 157–172.

Laird, D.A. (2006). Influence of layer charge on swelling of smectites. *Applied Clay Science*, *34*, 74–87. https://doi.org/10.1016/j.clay.2006.01.009

Lantenois, S., Lanson, B., Mulle, F., Bauer, A., Jullien, M., & Plançon, A. (2005). Experimental study of smectite interaction with metal Fe at low temperature: 1. Smectite destabilization. *Clays and Clay Minerals*, *53*, 597–612. https://doi.org/10.1346/CCMN.2005.0530606

Latta, D.E., Neumann, A, Premaratne, W.A.P.J., & Scherer, M.M. (2017). Fe(II)–Fe(III) electron 1 transfer in a clay mineral with low Fe content. *ACS Earth Space Chemistry*, *1*, 197–208. https://doi/10.1021/acsearthspacechem.7b00013

Le Forestier, L., Muller, F., Villiéras, F., & Pelletier, M. (2010). Textural and hydration properties of a synthetic montmorillonite compared with a natural Na-exchanged clay analogue. *Applied Clay Science*, *48*, 18–25. https://doi.org/10.1016/j.clay.2009.11.038

Lorimer, G.W., & Cliff, G. (1976). Analytical electron microscopy of minerals. In H. R. Wenk (ed), *Electron Microscopy in Mineralogy* (pp. 506–519). Berlin: Springer Verlag.

Ma, C., Fitzgerald, J.D., Eggleton, R.A., & Llewellyn, D.J. (1998). Analytical election microscopy in clays and other phyllosilicates: Loss of elements from a 90-nm stationary beam of 300-keV electrons. *Clays and Clay Minerals*, *46*, 301–316. https://doi.org/10.1346/CCMN.1998.0460309

Madejová, J., Komadel, P., & Čičel, B. (1994). Infrared study of octahedral site populations in smectites. *Clay Minerals*, *29*, 319–326. https://doi.org/10.1180/claymin.1994.029.3.03

McKinley, J.P., Zachara, J.M., Smith, S.C., & Turner, G.D. (1995). The influence of uranyl hydrolysis and multiple site-binding reactions on adsorption of U(VI) to montmorillonite. *Clays and Clay Minerals*, *43*, 586–598. https://doi.org/10.1346/CCMN.1995.0430508

Mermut, A.R., & Cano, A.F. (2001). Baseline studies of the Clay Minerals Society source clays: chemical analyses of major elements. *Clays and Clay Minerals*, *49*, 381–386. https://doi.org/10.1346/CCMN.2017.064065

Moll, W.R. (2001). Baseline studies of the Clay Minerals Society source clays: geological origin. *Clays and Clay Minerals*, *49*, 374–380. https://doi.org/10.1346/CCMN.2001.0490503

Newman, A.C.D., & Brown, G. (1987). The chemical constitution of clays. In A. C.D. Newman (ed), *Chemistry of Clays and Clay Minerals Monograph 6* (pp. 1–128), Mineralogical Society, London. Longman Scientific & Technical, Harlow, Essex, UK.

Nieto, F. (2002). Characterization of coexisting NH_4- and K-micas in very low-grade metapelites. *American Mineralogist*, *87*, 205–216. http://doi.org/10.2138/am-2016-5301

Nieto, F., Arroyo, X., & Aróstegui, J. (2016). XRD-TEM-AEM comparative study of n-alkylammonium smectites and interstratified minerals in shallow-diagenetic carbonate sediments of the Basque-Cantabrian Basin. *American Mineralogist*, *101*, 385–398. https://doi.org/10.2138/am-2016-5301

Perdrial, J.N., & Warr, L.N. (2011). Hydration behavior of MX80 Bentonite in a confined-volume system: implications for backfill design. *Clays and Clay Minerals*, *59*, 640–653. https://doi/10.1346/CCMN.2011.0590609

Podlech, C., Matschiavelli, N., Peltz, M., Kluge, S., Arnold, T., Cherkouk, A., Meleshyn, A., Grathoff, G., & Warr, L.N. (2021). Bentonite alteration in batch reactor experiments with and without organic supplements: implications for the disposal of radioactive waste. *Minerals*, *11*, 932. https://doi.org/10.3390/min11090932.

Qiao, Z., Liu, Q. & Zhang, S., & Wu, Y. (2019). The mineralogical characteristics between opaline silica in bentonite and α-cristobalite. *Solid State Sciences*, *96*, 105948. https://doi.org/10.1016/j.solidstatesciences.2019.105948

Steudel, A., Batenburg, L.F., Fischer, H.R., Weidler P.G., & Emmerich, K. (2009). Alteration of swelling clay minerals by acid activation. *Applied Clay Science*, *44*, 105–115. https://doi.org/10.1016/j.clay.2009.02.001

https://doi.org/10.1017/cmn.2024.20 Published online by Cambridge University Press

Sudheer Kumar, R., Podlech, C., Grathoff, G., Warr, L.N., & Svensson, D. (2021). Thermally induced bentonite alterations in the SKB ABM5. *Minerals*, *11*, 1017. https://doi.org/10.3390/min11091017.

Ufer, K., Kleeberg, R., Bergmann, J., & Dohrmann, R. (2012). Rietveld refinement of disordered illite-smectite mixed-layer structures by a recursive alogorithm. II: Powder-pattern refinement and quantitative phase analysis. *Clays and Clay Minerals*, *60*, 535–552. https://doi.org/10.1346/CCMN.2012.0600508

van der Pluijm, B.A., Lee. J.H., & Peacor, D.R. (1988). Analytical electron microscopy and the problem of potassium diffusion. *Clays and Clay Minerals*, *36*, 498–504.

van Olphen, H., & Fripiat, J.J. (1979). *Data Handbook for Clay Minerals and other Non-metallic Minerals* (346 pp.). Pergamon Press, Oxford.

Vantelon, D., Pelletier, M., Michot, L. J., Barres, O., & Thomas, F. (2001). Fe, Mg and Al distribution in the octahedral sheet of montmorillonites. An infrared study in the OH- bending region. *Clay Minerals*, *36*, 369–379. https://doi.org/10.1180/000985501750539463

Villar, M.V. (2005). MX-80 bentonite. Thermo-hydro-mechanical characterisation performed at CIEMAT in the context of the prototype project. *Informes Técnicos Ciemat*, *1053*, 39.

Villar, M.V., García-Siñeriz, J.L., Bárcena, I., & Lloret, A. (2005). State of the bentonite barrier after five years operation of an in situ test simulating a high level radioactive waste repository. *Engineering Geology*, *80*. https://doi.org/10.1016/j.enggeo.2005.05.001

Vogt, C., Lauterjung, J., & Fischer, R.X. (2002). Investigation of the clay fraction (<2 μm) of the clay minerals society reference clays. *Clays and Clay Minerals*, *50*, 388–400.

Wang, G., Wang, H., & Wen, J. (2019). Identification of interstratified mica or pyrophyllite monolayer from chlorite using advanced scanning/transmission electron microscopy. *American Mineralogist*, *104*, 1436–1443. https://doi.org/10.2138/am-2019-7074

Warr, L.N., & Nieto, F. (1998). Crystallite thickness and defect density of phyllosilicates in low-temperature metamorphic pelites; a TEM and XRD study of clay-mineral crystallinity-index standards. *The Canadian Mineralogist*, *36*, 1453–1474.

Warr, L.N. (2020). Recommended abbreviations for the names of clay minerals and associated phases. *Clay Minerals*, *55*, 261–264. https://doi.org/10.1180/clm.2020.30

Whitney, G., & Northrop, H.R. (1988). Smectite to illite reaction. Mechanism of illitization of bentonites in the geothermal fields. *American Mineralogist*, *73*, 77–90.

Wilson, M.J. (2013). Sheet silicates: clay minerals. In A. Deer, R.A. Howie, & J. Zussman (eds), *Rock Forming Minerals*, vol. *3C*, 2nd edn, 736 pp. Geological Society of London. ISBN 978-1-86239-359-2

Zou, Y.-C., Mogg, L., Clark, N., Bacaksiz, C., Milovanovic, S., Sreepal, V., Hao, G.-P., Wang, Y.-C., Hopkinson, D.G., Gorbachev, R., Shaw, S., Novoselov, K. S., Raveendran-Nair, R., Peeters, F.M., Lozada-Hidalgo, M., & Haigh, S.J. (2021). Ion exchange in atomically thin clays and micas. *Nature Materials*, *20*, 1677–1682. https://doi.org/10.1038/s41563-021-01072-6

Zviagina, B.A., McCarty, D.K., Środoń, J., & Drits, V.A. (2004). Interpretation of infrared spectra of dioctahedral smectites in the region of OH-stretching vibrations. *Clays and Clay Minerals*, *52*, 399–410. https://doi.org/10.1346/CCMN.2004.0520401

https://doi.org/10.1017/cmn.2024.20 Published online by Cambridge University Press